Tropical Cyclone Tilt and Precession in Moderate Shear: Precession Hiatus in a Critical Shear Regime

CHAU-LAM YU,[a] BRIAN TANG,[a] AND ROBERT G. FOVELL[a]

[a] *Department of Atmospheric and Environmental Sciences, University at Albany, State University of New York, Albany, New York*

(Manuscript received 12 September 2022, in final form 9 December 2022)

ABSTRACT: One source of uncertainty associated with vertical wind shear (VWS) on tropical cyclone (TC) intensity evolution arises when the VWS becomes sufficiently strong such that the TC vortex is unable to overcome the inhibiting effects of VWS (the critical shear regime), resulting in a transition from vortex realignment and eventual reintensification to persistent vortex misalignment and failure of reintensification. To uncover the initiation mechanism of the behavioral transition, this study examines the dynamical evolution of the vortex tilt and precession through a set of CM1 ensemble simulations in moderate shear (7.5 m s^{-1}) that includes the behavioral transition by systematically enhancing the TC vorticity amplitude aloft (vortex resiliency) at a restart point. In this critical shear regime, all experiments exhibit a common precession hiatus behavior, during which the tilt magnitude increases and later leads to divergent outcomes in intensity and tilt evolutions. Volume-averaged horizontal vorticity budget reveals an anomalous differential vorticity flux that emerges in the downtilt-left quadrant during the hiatus period. This differential vorticity flux generates horizontal vorticity that points toward the downtilt-right direction, simultaneously increasing the vortex tilt and slowing down the precession rate. This downtilt-left differential vorticity flux is due to midlevel vortex stretching at the rainband terminus region, where there is a transition from convective to stratiform precipitation. Meanwhile, the downdraft associated with stratiform precipitation also causes vorticity compression at the low levels. These results indicate that the stratiform rainband region is important for increasing the vortex tilt and pausing the precession.

KEYWORDS: Hurricanes/typhoons; Intensification; Mesoscale processes; Wind shear; Tropical cyclones

1. Introduction

Vertical wind shear (VWS) is one of the most influential environmental controls on the tropical cyclone (TC) structural development and intensification (DeMaria and Kaplan 1994). While strong VWS is generally hostile for TC development and intensification (DeMaria and Kaplan 1994; Kaplan and DeMaria 2003; Molinari et al. 2004; Paterson et al. 2005; Hendricks et al. 2010; Zhang and Tao 2013; Tao and Zhang 2015; Rios-Berrios and Torn 2017), moderate VWS (4.5–11.0 m s^{-1}; Rios-Berrios and Torn 2017) can cause significant uncertainties in TC intensity evolution and the onset of intensification, due to the nonlinear interactions between misaligned vortex structure, asymmetric convection and precipitation, and environmental flow (Zhang and Tao 2013; Bhatia and Nolan 2013; Rios-Berrios et al. 2018). Thus, TCs embedded in a moderate shear pose a great challenge for accurate intensity forecasts (DeMaria et al. 2005; Bhatia and Nolan 2013; Finocchio and Majumdar 2017).

VWS tilts a TC by advecting the upper-level center of circulation toward the downshear direction. The tilted vortex increases low-level convergence downshear, resulting in an asymmetric moisture distribution and secondary circulation with enhanced upward motion downshear (Raymond 1992; Jones 1995, 2000; Frank and Ritchie 1999, 2001; Reasor et al. 2013; DeHart et al. 2014; Rios-Berrios and Torn 2017; Schecter 2022). Simultaneously, there is descent and a suppression of convection upshear (Chen et al. 2006; Boehm and Bell 2021). The result is an asymmetric, wavenumber-1 pattern of rainband convection, where active convection initiates at the downshear-right (DR) quadrant, becomes mature downshear left (DL) and transitions into stratiform precipitation farther downwind. This asymmetric convection and precipitation subsequently propagate cyclonically following the vortex tilt (Ryglicki et al. 2018b; Rios-Berrios et al. 2018; Hazelton et al. 2020; Fischer et al. 2021). This relationship between shear, vortex tilt, and asymmetric convection has been frequently identified in observations (Reasor et al. 2000; Corbosiero and Molinari 2002; Chen et al. 2006; Reasor and Eastin 2012; Reasor et al. 2013; DeHart et al. 2014) and modeling simulations (DeMaria 1996; Wang and Holland 1996; Frank and Ritchie 2001).

For sheared, intensifying TCs, the vortex tilt vector can precess cyclonically toward the upshear quadrants before vortex realignment and intensification occurs (Tao and Zhang 2014; Rios-Berrios et al. 2018). A tilted vortex can be interpreted as the superposition of a mean axisymmetric vortex centered at the midlevel centroid and a pair of opposite-signed vorticity anomalies uptilt and downtilt at both low and upper levels (see Fig. 3 of Reasor and Montgomery 2001). Early studies interpreted the dynamics of cyclonic precession of vortex tilt as linear (Reasor and Montgomery 2001; Schecter et al. 2002; Reasor et al. 2004; Reasor and Montgomery 2015) and nonlinear advection (Polvani 1991) between the mean axisymmetric vortex and the upper- and low-level vorticity anomalies. For small vortex tilt, the linear advection of PV anomalies by the axisymmetric-mean vortex is shown to have dominant contribution to the cyclonic precession (Reasor and Montgomery 2001; Schecter et al. 2002). Based on dry dynamics, Reasor et al. (2004) later developed a heuristic model to explain the temporal

Corresponding author: Chau-Lam Yu, cyu7@albany.edu

DOI: 10.1175/JAS-D-22-0200.1

evolution of the small-amplitude tilt of a sheared TC vortex. This model demonstrated the existence of a left-of-shear, stable vortex tilt configuration, and they argued that the vortex realignment process can occur in dry dynamics via vortex Rossby wave (VRW) damping.

In bridging the gap between dry, sheared vortex dynamics and moist processes, Schecter and Menelaou (2020) and Schecter (2022) examined the vortex misalignment evolution in a shear-free environment. They found that vortex misalignment in preintensifying TCs is mostly governed by midtropospheric vorticity generation associated with the strong asymmetric convection distant from the surface circulation center. Adiabatic nondivergent advection of coherent vorticity features and lateral mixing can subsequently cause regrowth of vortex tilt, resulting in a nonmonotonic tilt evolution. As the TC intensifies and develops a strong radial vorticity gradient, VRW dynamics can contribute increasingly to the misalignment evolution (Schecter 2015), particularly in the mature hurricane stage.

The interplay between vertical wind shear, vortex tilt, and the diabatic moist process can result in a more complex vortex realignment process. In examining the tilt evolution of sheared TCs in full-physics simulations, several studies (Rios-Berrios et al. 2018; Nguyen and Molinari 2015; Chen et al. 2018) suggested that the evolution of the asymmetric precipitation centroid and the subsequent development of a deep subvortex within the misaligned parent cyclone are essential to the realignment process, consistent with other studies that highlight the importance of the midlevel vortex in early stage TC development (Raymond et al. 2014; Gjorgjievska and Raymond 2014). A "bottom-up" pathway has also been identified where alignment can occur due to vorticity generation from deep moist convection without a clear cyclonic precession (Miyamoto and Nolan 2018; Alvey et al. 2020). While questions remain about the mechanism that causes vortex realignment, studies have found that prolonged misalignment and the lack of intensification are typically associated with asymmetric, downtilt convection away from the surface circulation center (Rios-Berrios et al. 2018; Miyamoto and Nolan 2018; Alvey et al. 2020; Schecter and Menelaou 2020; Schecter 2020, 2022). Whereas rapid intensification onset is linked to the symmetrization of convective activity and precipitation, particularly in the upshear quadrants, to promote a more symmetric latent heating distribution and intensification of the TC circulation (Stevenson et al. 2014; Chen and Gopalakrishnan 2015; Rogers et al. 2016; Rios-Berrios et al. 2016a,b; Wadler et al. 2018).

Multiple modeling studies (Tao and Zhang 2015; Rios-Berrios et al. 2018; Rios-Berrios 2020; Alvey et al. 2020; Alland et al. 2021a,b) have examined the uncertainty in the intensification onset timing associated with the variability in the vortex precession rate and trajectory. This variability is linked to mesoscale differences, such as the vortex structure, convection, and moisture distribution. Another source of uncertainty arises when the TC vortex is nearly unable to overcome the inhibiting effects of vertical wind shear, hereafter referred as the critical shear regime. The existence of such a critical transition has been demonstrated in previous studies. For instance, Tao and Zhang (2015) showed in their simulations that all ensemble members transition from delayed (rapid) intensification to complete failure of intensification when the VWS magnitude increases from 6 to 7.5 m s^{-1}. The simulation results from Alland et al. (2021a,b) similarly indicate that such critical shear regime lies between 5 and 10 m s^{-1}, depending on the environmental relative humidity.

This behavioral transition from intensification to weakening near the critical shear regime likely depends on the TC environment and the vortex structure. For instance, Finocchio and Rios-Berrios (2021) performed an ensemble set of idealized simulations with increasing shear applied to different stages of a TC, and showed that the critical shear regime depends on storm size and structure. A stronger, deeper vortex is more resilient to shear and thus more likely to intensify in moderate wind shear (Rios-Berrios and Torn 2017). Environmental factors, such as relative humidity (Alland et al. 2021a,b), the shear profile (Onderlinde and Nolan 2017; Finocchio et al. 2016; Ryglicki et al. 2018a,b), TC outflow structure (Elsberry and Jeffries 1996; Black and Anthes 1971; Ryglicki et al. 2019; Dai et al. 2019, 2021), and sea surface temperature (Schecter 2022), also can influence the behavioral transition near the critical shear regime. For instance, Ryglicki et al. (2018a,b) demonstrated that for moderate shear the storm intensity evolution can diverge between failing and succeeding in realignment and intensification, depending on how deep the shear profile is, consistent with the findings of Onderlinde and Nolan (2017) and Finocchio et al. (2016). The existence of a critical transition is also consistent with the theoretical behavior of a ventilated TC (Tang and Emanuel 2010), in that if the strength of ventilation is increased beyond a certain threshold, only weakening solutions exist. Clearly, there is much complexity in reality. Here, we seek to avoid some of the complexity through a set of idealized simulations to gain fundamental understanding of how the behavioral transition modifies the precession trajectory, what mesoscale features determine this behavioral transition near the critical shear regime, as well as the mechanism leading to such transition, which have not been previously investigated in detail.

As will be seen, a defining feature near the critical shear regime is a "precession hiatus," marked by an increase in tilt magnitude and decrease in cyclonic precession rate, that occurs in the downshear-left quadrant. Our main goal in this study is to examine the dynamical processes and mesoscale features that cause the *onset of this precession hiatus*. Thus, the focus will be on the period *before* the behavioral transition near this critical shear regime, because this early, transient period has interesting behavior that is important for understanding the subsequent TC tilt and intensity evolution. A subsequent study will focus on the behavioral transition itself and divergent outcomes. To investigate the behavioral transition near critical shear regime, this paper examines the tilt and precession evolutions of a perturbed set of idealized TC simulations where the vortex resiliency is systematically enhanced by strengthening the mid- to upper-level vorticity using a nonlinear balanced perturbation method. The tilt and precession dynamics are then examined through detailed analyses of the horizontal and vertical vorticity budgets.

TABLE 1. Parameterization schemes used in the CM1 simulations.

Categories	Parameterization schemes	References
Microphysics	Morrison double-moment	Bryan and Morrison (2012)
Radiation	RRTMG longwave and shortwave	Iacono et al. (2008)
PBL	Yonsei University (YSU)	Hong et al. (2006)
Surface fluxes	Bulk aerodynamic formulas	Fairall et al. (2003), Donelan et al. (2004), Drennan et al. (2007)
Turbulence	CM1 simple PBL parameterization	Bryan and Rotunno (2009), Bryan (2012)

2. Methodology

a. Numerical model

In this study, we used the Cloud Model 1 (CM1; Bryan and Fritsch 2002), version 20.1, to perform convection-permitting, idealized simulations of tropical cyclones. The model is configured on an f plane with a Coriolis parameter set to 5×10^{-5} s^{-1} (20°N). The horizontal grid contains an inner 728 × 728 km^2 region with uniform 2-km grid spacing. Beyond this uniform region, the spacing is gradually increased from 2 to 16 km at the outer portion of the domain, with a total domain size of 1520 × 1520 km^2 and periodic lateral boundary conditions. The vertical grid has 59 levels in total, with variable spacing that increases from 25 to 500 m within the lowest 5500 m, above which the spacing becomes uniform at 500 m. The model top is set at 25 km. The parameterization schemes employed are listed in Table 1.

All experiments in this study are initialized using the moist tropical sounding from Dunion (2011) with a sea surface temperature of 28°C. Below 850 hPa, the RH structure is the same as the Dunion moist tropical sounding, while above 850 hPa, the RH is constant at 50% throughout the entire domain, similar to Alland et al. (2021a). The analytic Rotunno and Emanuel (1987) vortex is used to initialize all experiments. The initial vortex wind profile has a maximum wind speed of 15 m s^{-1} at the radius of maximum wind (RMW) of 82.5 km, and radially decreases outward to 0 m s^{-1} at 412.5-km radius. The wind decreases linearly with height to 0 m s^{-1} at z = 15 km.

Following Alland et al. (2021a), a large-scale nudging method is used to introduce VWS in all experiments. The environment has no VWS during the first 12-h period to spin up the TC convection and structure. After this 12-h spinup period, VWS is added by nudging the horizontal wind field toward prescribed background wind profiles, with nudging time scale τ = 3 h. The prescribed wind profile is zonal, with −2 m s^{-1} wind for z < 1.5 km and a linear westerly shear between z = 1.5 and 12 km, above which the wind is constant with a magnitude depending on the shear value. The background wind gradually strengthens to the prescribed profile roughly by 24 h, which is then held constant throughout the rest of the simulation. Once the background wind profile is applied, the TC begins to translate in the direction of the background mean flow. To keep the TC inner core within the high-resolution inner domain, the CM1 model domain moves following the TC center, using the same moving domain strategy as in Alland et al. (2021a,b).

b. Perturbation simulations

Alland et al. (2021a,b) investigated the combined effect of midlevel dry air and VWS on modulating TC development via different ventilation pathways using a set of idealized ensemble simulations with various combinations of moisture profiles and wind shear magnitudes. Their ensemble simulations show that a behavioral transition occurs between the 5 and 10 m s^{-1} shear members. To examine this behavioral transition more closely, and to find the critical shear regime, simulations are performed with the wind shear magnitude incremented from 5.5 to 9 m s^{-1}. The simulated storms still intensify for a VWS < 7.0 m s^{-1}, albeit more slowly as the shear increases. For a VWS of 7.5 m s^{-1}, however, the TC fails to intensify. Hereafter, we will refer to this 7.5 m s^{-1} shear experiment as the control experiment (CTRL).

Previous studies indicated that the size, structure, and initial intensity of a TC can influence the critical shear value at which the storm fails to intensify. Finocchio and Rios-Berrios (2021) showed this dependence in a set of idealized simulations with increasing shear applied at different stages of a base TC simulation. Rios-Berrios and Torn (2017) also showed that a TC vortex with a stronger and deeper vorticity structure is more resilient to the inhibiting effects of shear and more likely to intensify, consistent with the results of Jones (1995). Given this knowledge, our goal in this study is to examine how this transitional behavior near the critical shear regime emerges as we vary the strength of the TC vortex aloft. To this end, we introduce an inner-core vorticity enhancement to the CTRL experiment by adding an axisymmetric vorticity perturbation after the 12-h spinup period using a balanced perturbation method, which will be detailed in section 2c. This axisymmetric vorticity perturbation $\zeta'(r, z)$ is obtained by multiplying an analytic amplification factor $\Upsilon(r, z)$ to the axisymmetric mean vorticity $\zeta_0(r, z)$ of the CTRL experiment at 12 h:

$$\Upsilon(r, z) = \frac{\alpha}{100}\exp\left[-\left(\frac{z - 9500}{5000}\right)^2\right]\exp\left[-\left(\frac{r}{75\,000}\right)^6\right],$$
$$\zeta'(r, z) = \Upsilon(r, z) \times \zeta_0(r, z). \quad (1)$$

The value of $\zeta_0(r, z)$ is obtained by performing azimuthal average with respect to the domain (TC) center. $\Upsilon(r, z)$ has a Gaussian vertical profile that attains a maximum of α/100 at z = 9.5 km and decreases to 0 outside of 75-km radius. Here α denotes the vorticity amplification (in percent). As an example, the azimuthal mean structures for the unperturbed and perturbed vertical vorticity, as well as the vorticity anomaly

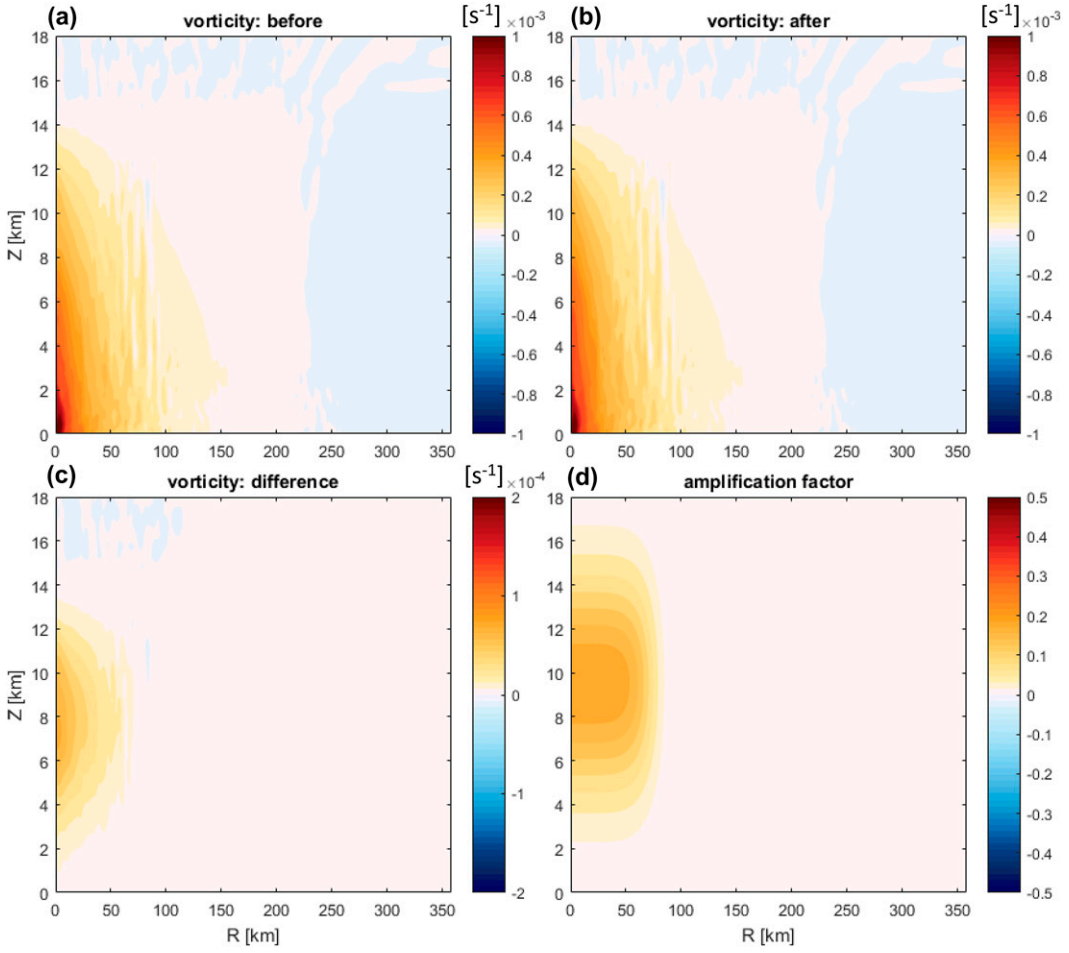

FIG. 1. Radius–height plot of the azimuthal mean vorticity after the 12-h spinup period (a) before and (b) after the vorticity perturbation is added, (c) the corresponding difference, and (d) the amplification factor for $\alpha = 20$.

and the amplification factor $\Upsilon(r, z)$, for $\alpha = 20$ are shown in Fig. 1. After obtaining vorticity perturbation $\zeta'(r, z)$, the corresponding balanced pressure and temperature perturbations are diagnosed using the technique discussed in the next subsection. The perturbation fields are then added to the 12-h CTRL fields, and then the simulation is restarted, to create a set of α-perturbation experiments. Including the CTRL ($\alpha = 0$), we created a four-member set of experiments with $\alpha = 0$, 10, 20, and 40. Throughout the paper, the perturbed experiments would be referred as "αXX" with "XX" being the corresponding enhancement percentage.

c. *Balanced vorticity perturbation*

The balanced perturbation method diagnoses the pressure and thermal perturbations that are required to satisfy the nonlinear balance equation (NLBE; Charney 1955; Krishnamurti 1968; Haltiner and Williams 1980; Davis and Emanuel 1991; Raymond 1992) and hydrostatic balance:

$$\nabla \cdot (c_p \theta_\rho \nabla \pi) = 2(\psi_{xx}\psi_{yy} - \psi_{xy}^2) + f\nabla^2\psi, \tag{2}$$

$$c_p \theta_\rho \frac{\partial \pi}{\partial z} = g\frac{\theta_\rho - \theta_{\rho 0}}{\theta_{\rho 0}}, \tag{3}$$

where π is the Exner function, $c_p = 1005.7$ J kg^{-1} K^{-1} is the specific heat of dry air at constant pressure, θ_ρ *is* the density potential temperature, $\theta_{\rho 0}$ is reference profile of density potential temperature used in the CM1 model, f is the Coriolis parameter, and ψ is the streamfunction of the nondivergent wind. The NLBE (2) is a diagnostic equation for π given a vorticity structure represented by the streamfunction ψ.

As derived in appendix A, perturbations are introduced to a model state in a balanced manner based on (2) and (3), such that the unbalanced part of the original flow is largely unaffected after the perturbation is added. This yields a set of balanced equations for the perturbation fields,

$$c_p \nabla \cdot \theta_{\rho 2} \nabla \pi' + c_p \nabla \cdot \theta'_\rho \nabla \pi_1 = f\nabla^2\psi' + 2(\psi'_{xx}\psi_{1yy} + \psi_{1xx}\psi'_{yy} + \psi'_{xx}\psi'_{yy} - 2\psi'_{xy}\psi_{1xy} - \psi'^2_{xy}), \tag{4}$$

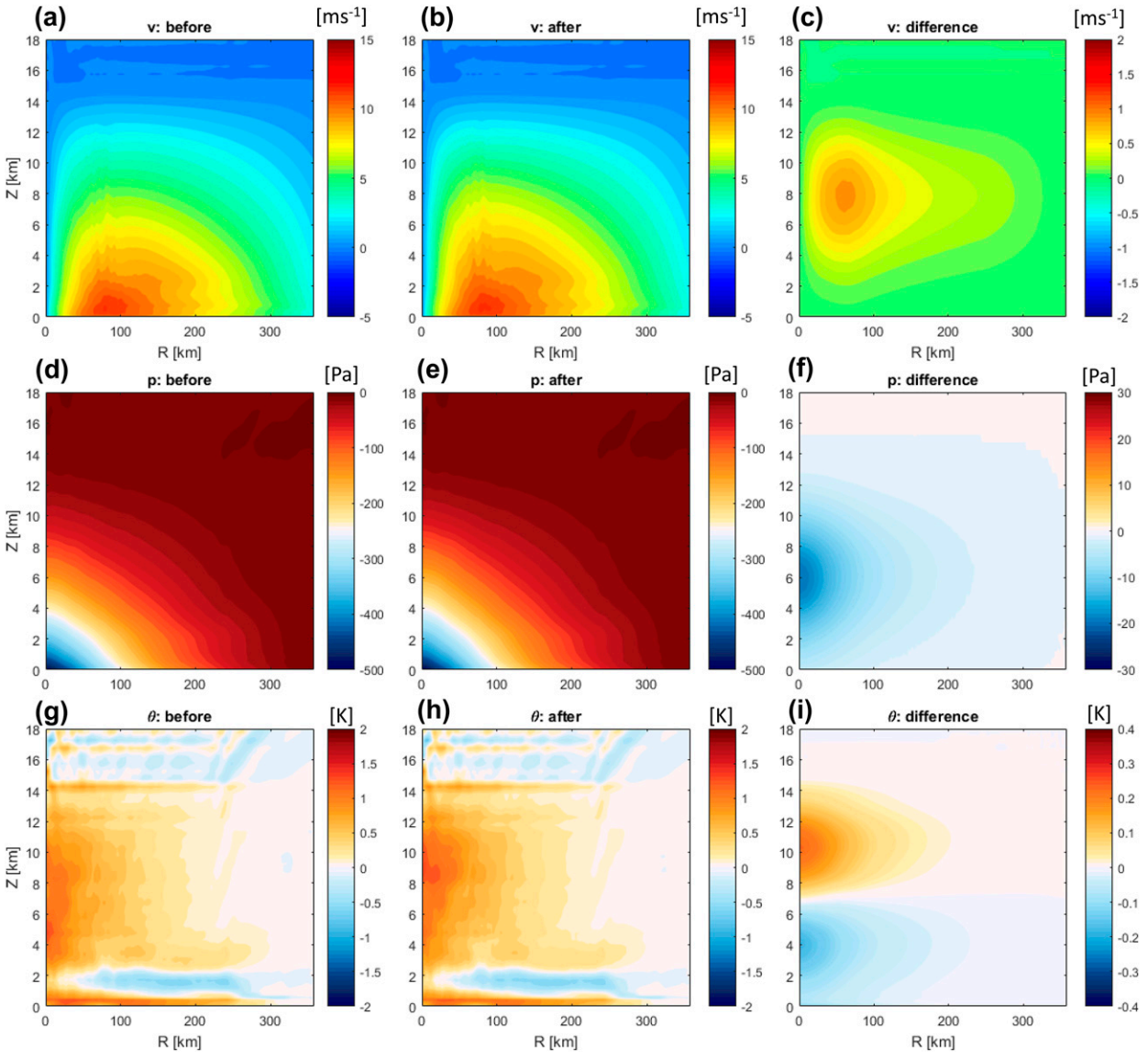

FIG. 2. Azimuthal mean plots of the (a)–(c) tangential wind, (d)–(f) pressure anomaly, and (g)–(i) potential temperature anomaly of the $\alpha 20$ experiment. (left) Unperturbed fields at $t = 12$ h, (center) perturbed fields, and (right) the perturbation.

$$\theta'_\rho \left[c_p \frac{\partial(\pi' + \pi_1)}{\partial z} - \frac{g}{\theta_{\rho 2}} \right] = -c_p \theta_{\rho 1} \frac{\partial \pi'}{\partial z}, \tag{5}$$

where all perturbation quantities are represented by the prime symbol, variables with subscript 1 denote the original fields, and variables with subscript 2 denote fields after the perturbations are introduced, i.e., $q_2 = q_1 + q'$ with q being a generic variable. After solving for the balanced θ'_ρ and π', the water vapor mixing ratio is adjusted such that relative humidity is unchanged. Hydrometeors, however, are not adjusted. As an example, Fig. 2 shows the azimuthally averaged tangential wind before (Fig. 2a) and after (Fig. 2b) the introduction of the vorticity perturbation for $\alpha 20$, which has a maximum tangential wind increment of about 2 m s^{-1} near a height of 8 km (Fig. 2c). The corresponding pressure perturbation (Fig. 2f) is most negative around 6 km, with a warm and cold potential temperature θ perturbation above and below 7 km (Fig. 2i).

d. *Measures of the TC vortex tilt*

Our study employs the centroid-based methods discussed in Nguyen et al. (2014) and Ryglicki and Hart (2015) to determine the TC centers at a given level based on the vorticity centroid

$$\mathbf{x}_{\text{center}} = \frac{\int_0^{2\pi} \int_0^R \zeta_z \mathbf{x}\, r\, dr\, d\lambda}{\int_0^{2\pi} \int_0^R \zeta_z r\, dr\, d\lambda}, \tag{6}$$

where $\mathbf{x}$ is the position vector, λ is the azimuthal angle, ζ_z is the relative vorticity, and R is the radius of integration and is taken to be 120 km in this study. Following the procedure described in Nguyen et al. (2014), the location of the minimum pressure at each level is used as the initial guess of the center. Equation (6) is then computed to iteratively update the center. Thirty iterations are used to guarantee convergence of the center location. In this study, the tilt of the TC vortex is defined as the vector difference between the centers at $z = 6.5$ km and $z = 1.5$ km.

While the centroid-based definition of vortex tilt is intuitive, one deficiency is that it is relatively difficult to obtain a governing equation that can quantify its temporal evolution. To address this deficiency, we propose an alternative measure of the vortex tilt based on a volume averaged horizontal vorticity vector. Consider the vorticity field of a tilted vortex, which can be decomposed into the sum of a vertically aligned mean vortex $\overline{\zeta}_z$, centered at the midlevel vorticity centroid, and vorticity perturbations ζ_z', as shown in Fig. 3a. The tilted component of the vorticity field is entirely characterized by the vorticity perturbations, which consists of a pair of opposite-signed vorticity anomalies uptilt and downtilt. Furthermore, as a consequence of the nondivergence of the vorticity, the vertical gradient of vertical vorticity equals the convergence of horizontal vorticity:

$$\frac{\partial \zeta_z}{\partial z} = -\nabla \cdot \boldsymbol{\zeta}_h. \tag{7}$$

Because the vorticity anomalies uptilt and downtilt have opposite vertical gradients of ζ_z (Fig. 3a), there must be a divergence of $\boldsymbol{\zeta}_h$ uptilt and convergence of $\boldsymbol{\zeta}_h$ downtilt, and thus, $\boldsymbol{\zeta}_h$ points from the uptilt toward the downtilt region, as illustrated in Fig. 3b.

To support this conceptual illustration, Fig. 3c shows the 1.5–6.5-km vertically averaged $\boldsymbol{\zeta}_h$ vector field of the α20 experiment during 30–31 h. The 1.5- and 6.5-km circulations and centers are displaced from one another, indicative of the vortex tilt. The $\boldsymbol{\zeta}_h$ vectors are divergent uptilt and convergent downtilt, resulting in a volume-averaged $\boldsymbol{\zeta}_h$ (denoted as $\langle \boldsymbol{\zeta}_h \rangle$) pointed in approximately the same direction as the tilt (thick blue arrow in Fig. 3c). On the other hand, a vertically aligned vortex is characterized by a symmetric region of negative $\partial \zeta_z / \partial z$ owing to thermal wind balance, which is associated with symmetrically divergent $\boldsymbol{\zeta}_h$ vectors and, thus, zero $\langle \boldsymbol{\zeta}_h \rangle$. As we will see in section 4a, $\langle \boldsymbol{\zeta}_h \rangle$ is indeed positively correlated with the centroid-based vortex tilt both in terms of the magnitude and direction. Thus, $\langle \boldsymbol{\zeta}_h \rangle$ measures the tilt of the vorticity field within the volume, and importantly, the $\langle \boldsymbol{\zeta}_h \rangle$ budget equation can be used to diagnose controls on the tilt evolution.

e. Horizontal vorticity budget in a rotating coordinate

We now show how the horizontal vorticity budget equation can provide a framework for investigating TC tilt and precession mechanisms. Additionally, the equation is cast into a rotating coordinate system, yielding two equations that separately quantify the tendencies of the $\langle \boldsymbol{\zeta}_h \rangle$ magnitude and direction, representing the tilt magnitude and precession rate. Doing so has the advantage of a natural partitioning that can offer insight into tilt and precession mechanisms.

We start by defining a cylindrical volume centered at the midlevel vorticity centroid at $z = 4.5$ km with a radius of 120 km and is vertically bounded between $z = 1.5$ and 6.5 km (Fig. 4a). Other cylindrical volumes were also tested, and the obtained $\langle \boldsymbol{\zeta}_h \rangle$ were similar. Next, we define the unit vectors of a coordinate system that rotates following the direction of $\langle \boldsymbol{\zeta}_h \rangle$. Since $\langle \boldsymbol{\zeta}_h \rangle$ generally points along the direction of vortex tilt, we denote the unit vector along the $\langle \boldsymbol{\zeta}_h \rangle$ vector direction as $\hat{\mathbf{n}}$. The horizontal direction perpendicular to $\langle \boldsymbol{\zeta}_h \rangle$ is therefore $\hat{\mathbf{s}} = \hat{\mathbf{k}} \times \hat{\mathbf{n}}$, where $\hat{\mathbf{k}}$ is the vertical unit vector. The vector $(\hat{\mathbf{n}}, \hat{\mathbf{s}}, \hat{\mathbf{k}})$ therefore represents a coordinate system that rotates with time, such that $\hat{\mathbf{n}}$ always remains aligned with $\langle \boldsymbol{\zeta}_h \rangle$. Given this coordinate system, the horizontal vorticity vector field $\boldsymbol{\zeta}_h$ within the cylindrical volume can be written as $\boldsymbol{\zeta}_h = \zeta_n \hat{\mathbf{n}} + \zeta_s \hat{\mathbf{s}}$. Based on the definition of $\hat{\mathbf{n}}$, it follows that $\langle \boldsymbol{\zeta}_h \rangle = \langle \zeta_n \rangle \hat{\mathbf{n}}$ and $\langle \zeta_s \rangle \equiv 0$.

This coordinate system has several benefits. First, since $\hat{\mathbf{n}}$ is parallel to $\langle \boldsymbol{\zeta}_h \rangle$, the generation of ζ_n can only influence the magnitude of $\langle \boldsymbol{\zeta}_h \rangle$ (i.e., $\langle \zeta_n \rangle$), but not its direction. On the other hand, since $\hat{\mathbf{s}}$ is perpendicular to $\langle \boldsymbol{\zeta}_h \rangle$, changes of ζ_s field can only cause a deflection of the $\langle \boldsymbol{\zeta}_h \rangle$ direction, but not its magnitude $\langle \zeta_n \rangle$. Figure 4b illustrates these two properties of $\delta\zeta_n$ and $\delta\zeta_s$ by considering an incremental change $\boldsymbol{\delta\zeta}_h$ over a small-time increment δt. Therefore, the horizontal vorticity budget cast on the $(\hat{\mathbf{n}}, \hat{\mathbf{s}}, \hat{\mathbf{k}})$ coordinate yields the following two governing equations for $\langle \zeta_n \rangle$ and the precession rate of $\hat{\mathbf{n}}$ (denoted as Ω, positive for counterclockwise precession), as derived in appendix B:

$$\frac{d\langle \zeta_n \rangle}{dt} = -\left\langle \frac{\partial}{\partial z}(-\mathbf{v}_h \cdot \nabla_h v_s) \right\rangle - \left\langle \frac{\partial}{\partial z}\left(-w \frac{\partial v_s}{\partial z}\right) \right\rangle + \left\langle \frac{\partial}{\partial s}(-\mathbf{v} \cdot \nabla w) \right\rangle + f\left\langle \frac{\partial (v_n - v_{gn})}{\partial z} \right\rangle + \mathrm{Baro}^N + \mathrm{Frict}^N, \tag{8}$$

$$\Omega \langle \zeta_n \rangle = \left\langle \frac{\partial}{\partial z}(-\mathbf{v}_h \cdot \nabla_h v_n) \right\rangle + \left\langle \frac{\partial}{\partial z}\left(-w \frac{\partial v_n}{\partial z}\right) \right\rangle - \left\langle \frac{\partial}{\partial n}(-\mathbf{v} \cdot \nabla w) \right\rangle + f\left\langle \frac{\partial (v_s - v_{gs})}{\partial z} \right\rangle + \mathrm{Baro}^S + \mathrm{Frict}^S, \tag{9}$$

where $\partial/\partial n$ and $\partial/\partial s$ are the spatial derivatives along $\hat{\mathbf{n}}$ and $\hat{\mathbf{s}}$, respectively; $\mathbf{v}$ and $\mathbf{v}_h$ are the three-dimensional and horizontal wind velocities; v_{gn} and v_{gs} are the large-scale nudging wind profiles in the $\hat{\mathbf{n}}$ and $\hat{\mathbf{s}}$ directions; $\mathrm{Baro}^N = \langle \hat{\mathbf{n}} \cdot \nabla p \times \nabla \rho^{-1} \rangle$ and $\mathrm{Baro}^S = \langle \hat{\mathbf{s}} \cdot \nabla p \times \nabla \rho^{-1} \rangle$ are the baroclinic terms, where ρ is the density and p is the pressure; $\mathrm{Frict}^N = \langle \hat{\mathbf{n}} \cdot \nabla \times \mathbf{F} \rangle$ and $\mathrm{Frict}^S = \langle \hat{\mathbf{s}} \cdot \nabla \times \mathbf{F} \rangle$ are the frictional terms, where $\mathbf{F}$ is friction. The first three terms on the right-hand side of (8) and (9) represent $\boldsymbol{\zeta}_h$ generation due to differential horizontal and vertical advections, and horizontal gradient of w momentum advection. All the terms on right-hand side of (8) and (9) can generate differential circulation in the horizontal and vertical directions, contributing to the changes in $\langle \boldsymbol{\zeta}_h \rangle$ magnitude and the precession rate Ω of the $\langle \boldsymbol{\zeta}_h \rangle$ vector.

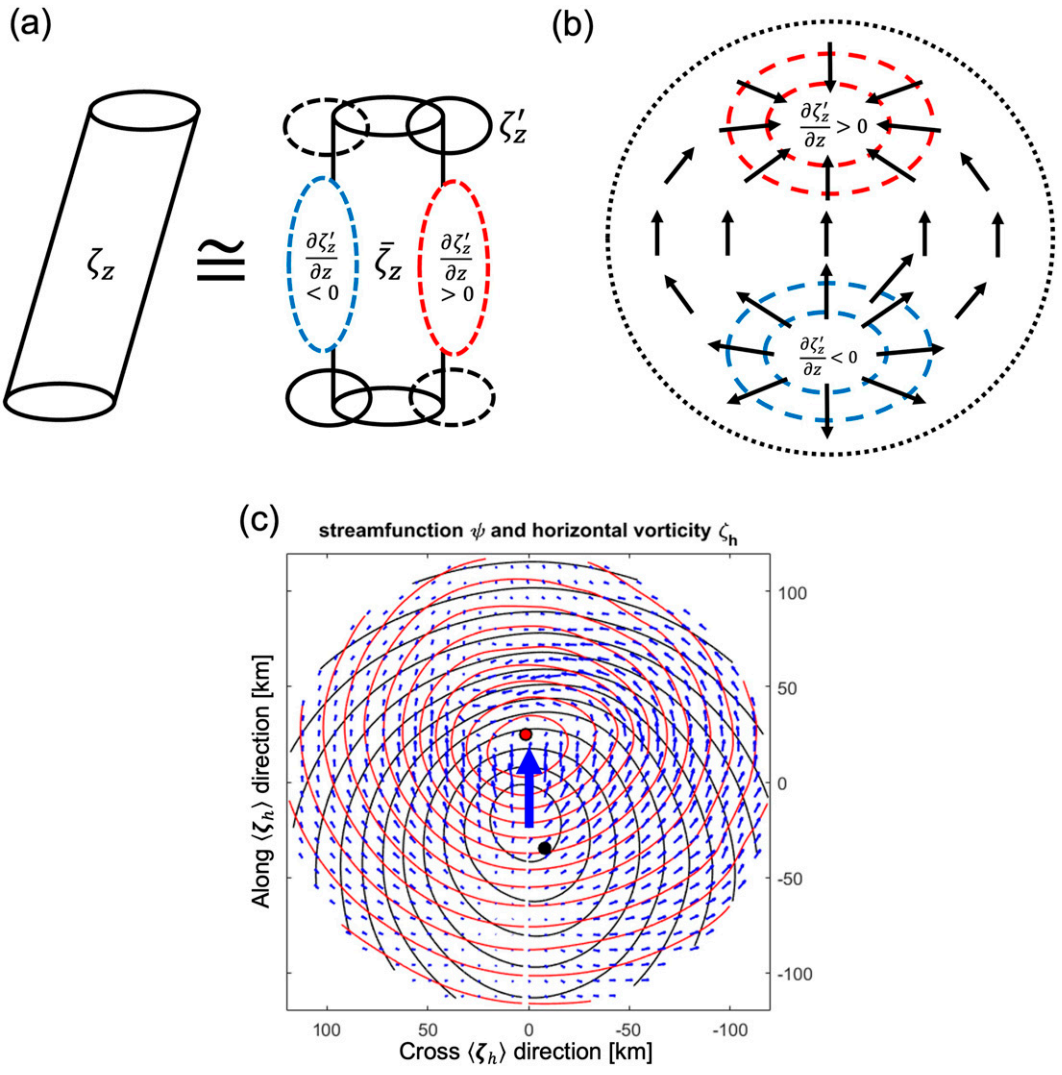

FIG. 3. For a tilted TC vortex, (a) the tilted vertical vorticity can be interpreted as the sum of a vertically aligned mean vortex centered at the midlevel centroid and pairs of opposite-signed vorticity perturbations uptilt and downtilt. The uptilt and downtilt vorticity perturbations have opposite vertical gradients, indicated by the red and blue dashed circles. (b) Schematic of the vertically averaged horizontal vorticity vector (black arrows) and regions of positive and negative vertical gradient of vorticity in the uptilt and downtilt regions. (c) For the $\alpha 20$ experiment, the 1.5-km streamfunction and vorticity centroid (black contours and dot) and 6.5-km streamfunction and vorticity centroid (red contours and dot), averaged between 30 and 31 h. All fields are rotated such that the volume-averaged horizontal vorticity vector points at the positive y direction. The vertically averaged horizontal vorticity field is shown by the short blue vectors, and the direction of the volume-averaged horizontal vorticity vector is shown by the long blue arrow.

Throughout the rest of this paper, all plan views in this coordinate will be oriented such that the $\hat{\mathbf{n}}$ points at positive y direction, as depicted in Fig. 4b.

Equations (8) and (9) are further partitioned into axial-mean and eddy contributions. Here, the axial mean of a variable is defined to be the azimuthal mean about the vorticity centroid *at each level*, i.e., following the tilt. Each term in (8) and (9) is then computed using only the axial-mean variables, then volume averaged, as denoted by $\langle \cdot \rangle_m$. This partition is useful since the symmetric part (with respect to vorticity centroid at each level) of the terms on the rhs of (8) and (9) strongly cancel. Such a cancellation obscures the interpretation of the net tendency. The axial-mean equations are

$$\frac{d\langle \zeta_n \rangle_m}{dt} = -\left\langle \frac{\partial}{\partial z}(-\mathbf{v}_h \cdot \nabla_h v_s) \right\rangle_m - \left\langle \frac{\partial}{\partial z}\left(-w \frac{\partial v_s}{\partial z}\right) \right\rangle_m + \left\langle \frac{\partial}{\partial s}(-\mathbf{v} \cdot \nabla w) \right\rangle_m + f\left\langle \frac{\partial (v_n - v_{gn})}{\partial z} \right\rangle_m + \mathrm{Baro}_m^N + \mathrm{Frict}_m^N, \tag{10}$$

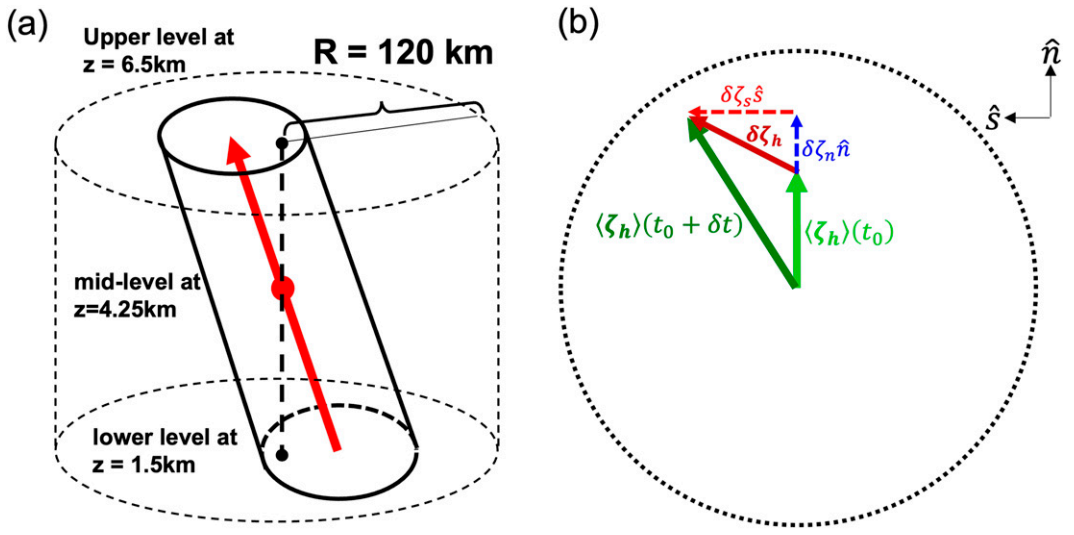

FIG. 4. (a) The volume averaged three-dimensional vorticity vector, given by the red vector, of a tilted TC vortex. The black dashed cylinder shows the $r = 120$ km volume that is centered at the midlevel (4.5-km) vorticity centroid for the volume integration. (b) Illustration of the coordinate system ($\hat{\mathbf{n}}$, $\hat{\mathbf{s}}$). The light green arrow indicates the volume-averaged horizontal vorticity vector $\langle\boldsymbol{\zeta}_h\rangle$ at a given time t_0, which points along $\hat{\mathbf{n}}$; the dark green arrow indicates $\langle\boldsymbol{\zeta}_h\rangle$ at $t_0 + \delta t$; the total vector change $\delta\boldsymbol{\zeta}_h$ over this δt period is represented by the dark red arrow, which can be decomposed into the $\hat{\mathbf{n}}$ and $\hat{\mathbf{s}}$ components, $\zeta_n\hat{\mathbf{n}}$ and $\zeta_s\hat{\mathbf{s}}$, as represented by blue dashed and red dashed arrows, respectively.

$$\langle\zeta_n\rangle\Omega_m = \left\langle\frac{\partial}{\partial z}(-\mathbf{v}_h\cdot\nabla_h v_n)\right\rangle_m + \left\langle\frac{\partial}{\partial z}\left(-w\frac{\partial v_n}{\partial z}\right)\right\rangle_m - \left\langle\frac{\partial}{\partial n}(-\mathbf{v}\cdot\nabla w)\right\rangle_m + f\left\langle\frac{\partial(v_s - v_{gs})}{\partial z}\right\rangle_m + \mathrm{Baro}_m^S + \mathrm{Frict}_m^S. \quad (11)$$

The eddy equations are then defined as the difference between the full Eqs. (8) and (9) and the axial-mean Eqs. (10) and (11), with $\langle\cdot\rangle_e$ referring to the eddy contribution, yielding

$$\frac{d\langle\zeta_n\rangle_e}{dt} = -\left\langle\frac{\partial}{\partial z}(-\mathbf{v}_h\cdot\nabla_h v_s)\right\rangle_e - \left\langle\frac{\partial}{\partial z}\left(-w\frac{\partial v_s}{\partial z}\right)\right\rangle_e + \left\langle\frac{\partial}{\partial s}(-\mathbf{v}\cdot\nabla w)\right\rangle_e + f\left\langle\frac{\partial v_n}{\partial z}\right\rangle_e + \mathrm{Baro}_e^N + \mathrm{Frict}_e^N, \quad (12)$$

$$\langle\zeta_n\rangle\Omega_e = \left\langle\frac{\partial}{\partial z}(-\mathbf{v}_h\cdot\nabla_h v_n)\right\rangle_e + \left\langle\frac{\partial}{\partial z}\left(-w\frac{\partial v_n}{\partial z}\right)\right\rangle_e - \left\langle\frac{\partial}{\partial n}(-\mathbf{v}\cdot\nabla w)\right\rangle_e + f\left\langle\frac{\partial v_s}{\partial z}\right\rangle_e + \mathrm{Baro}_e^S + \mathrm{Frict}_e^S. \quad (13)$$

Note the large-scale nudging terms, $f\langle\partial v_{gn}/\partial z\rangle$ and $f\langle\partial v_{gs}/\partial z\rangle$, are a constant forcing throughout the domain. Therefore, $f\langle\partial v_{gn}/\partial z\rangle_e$ and $f\langle\partial v_{gs}/\partial z\rangle_e$ are both zero.

3. Overview of model simulations

The tilt and intensity evolution of the simulations is now examined (Fig. 5). Starting from 12 h, when the shear is introduced, the storms in all the simulations exhibit a clear downshear tilt toward the east (Fig. 5a). After the tilt reaches a magnitude of about 50 km (when the radius of maximum wind is at 70 km), a cyclonic precession commences. However, the precession exhibits a pause while the tilt increases around 35–40 h in all the experiments, resulting in a kink in the precession trajectories, as highlighted by the black arrow in Fig. 5a. During this period, the vorticity field at 6.5 km is characterized by an inner-core maximum and an area of positive anomalies downtilt associated with rainband convection (not shown). The vorticity centroid, which tends to coincide well with the streamfunction minimum (Fig. 3c), shows a vertically coherent, downtilt displacement, rather than any discontinuities. During this hiatus initiation, the spread in the tilt (Fig. 5a) and intensity (Figs. 5b,c) are generally small among the experiments. In addition to the increase of tilt and pause of precession, the intensity of the storms remains steady between 40 and 50 h. However, by the end of the hiatus around 50 h, the experiments start to diverge. The tilt of the CTRL experiment continues to increase, and the intensity weakens, distinctly failing to resume the precession compared to other experiments (Fig. 5a). The $\alpha10$ experiment also weakens to a similar intensity as the CTRL, but can gradually resume the cyclonic precession after 80 h. The $\alpha20$ and $\alpha40$ experiments, on the other hand, have shorter precession trajectories, and the TCs in both simulations resume precessing more quickly. Toward the end of the simulation, these TCs become more aligned and intensify more quickly.

Given that the precession hiatus appears to be a common feature that occurs before the ensemble simulations diverge at later times, the emergence of precession hiatus could be a precursor feature that signals that the storm is near its critical

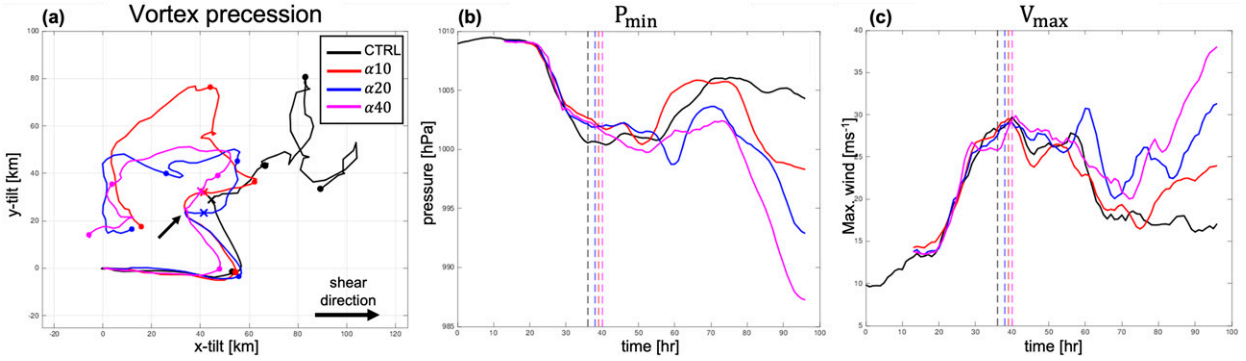

FIG. 5. (a) The vortex centroid tilt trajectories (6.5-km centroid relative to the 1.5-km centroid at the origin) of the simulations. Dots along the trajectories are plotted at 24-h intervals (the first dot is 12 h after the introduction of the wind shear). The crosses show the composite times. The black arrow indicates the kink feature in the precession trajectory (see text). (b),(c) The time series of the minimum sea level pressure and maximum 10-m wind, respectively. The vertical dashed lines show the composite times for each experiment.

shear regime and the future intensity evolution could be uncertain. To this end, the goals of the current study are to answer the following questions. Why does this precession hiatus occur? Specifically, what dynamical processes and mesoscale features are responsible for causing the pause in the precession and increase in the vortex tilt? We will use the horizontal vorticity budget equations introduced in section 2e to quantify the contributions of various processes to the tilt magnitude and precession evolution. The divergent storm evolutions that occur after the precession hiatus, on the other hand, will be examined in a subsequent study.

4. Horizontal vorticity analysis

In this section, we will examine the horizontal vorticity evolution and budget to understand the dynamics that lead to the increase in vortex tilt and the precession hiatus.

a. Correlation between vortex tilt and horizontal vorticity

First, we assess the use of the volume-averaged horizontal vorticity as an appropriate metric of the vortex tilt to complement the theoretical arguments in section 2d. Figure 6 shows scatterplots of the vortex tilt and volume averaged horizontal vorticity vector magnitudes (Fig. 6a) and directions (Fig. 6b) between 30 and 50 h when the vortex tilt increases. Significant, positive correlations in the magnitude (0.81) and direction (0.69) exist. The significant, positive correlations confirm the physical relationship between the tilted structure of vertical vorticity field and the horizontal vorticity vector (Figs. 3b,c), supporting that the volume-averaged horizontal vorticity may be used as a measure of the vortex tilt to understand the processes that lead to the precession hiatus. Throughout the rest of the study, we will use the term "precession" to refer to the precession of both the centroid-based vortex tilt vector and the volume-averaged horizontal vorticity vector.

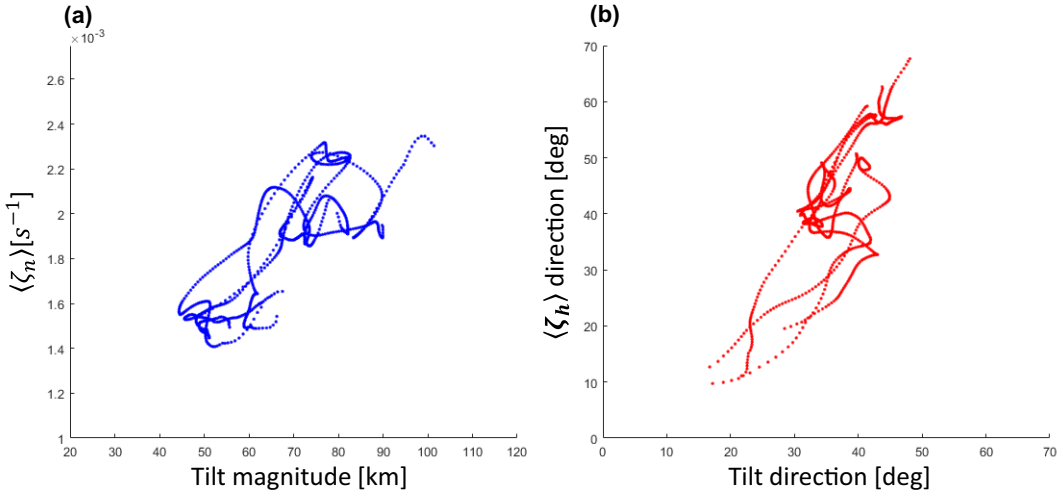

FIG. 6. Scatterplots of (a) the tilt magnitude and the volume-averaged horizontal vorticity magnitude and (b) the direction of the vortex tilt and the direction of the volume-averaged horizontal vorticity vector for all four experiments between 30 and 50 h, both measured counterclockwise from the east.

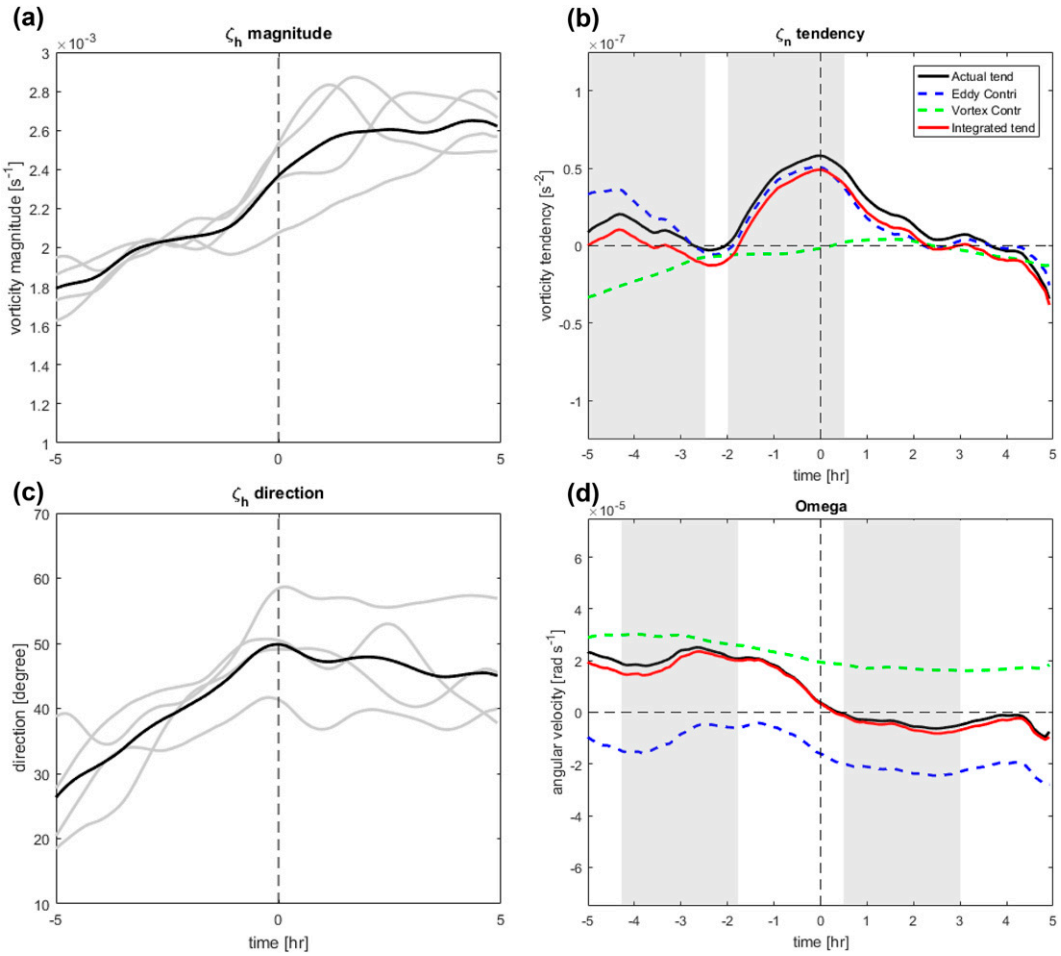

FIG. 7. Time series of the composite mean of all experiments: (a) magnitude of the volume-averaged horizontal vorticity vector $\langle\zeta_n\rangle$ (black), together with each experiment (gray); (b) horizontal vorticity tendency ($d\langle\zeta_n\rangle/dt$, solid black line), together with the averaged tendency (solid red line), eddy contribution (blue, dashed line), and axial-mean contribution (green, dashed line); (c) $\langle\zeta_h\rangle$ direction (black), together with each experiment (gray); (d) precession rate of $\langle\zeta_h\rangle$ (Ω, solid black line), together with the averaged precession rate (solid red line), eddy contribution (blue dashed line), and axial-mean contribution (green dashed line). The two gray shaded periods in (b) and (d) indicate the time periods used to examine changes in the $\langle\zeta_n\rangle$ tendency and Ω.

b. Horizontal vorticity budget evolution

To extract the common features across the experiments that emerge during the hiatus initiation, we will composite all members relative to the time when $\langle\zeta_n\rangle$ shows a clear increase during the precession hiatus. The times of each member are shown in the precession trajectory (cross symbols in Fig. 5a) and intensity time series (vertical dashed lines in Figs. 5b,c). From Fig. 5a, we see that these times are near or just after the emergence of the kinks in the precession trajectory.

As shown in Fig. 7a, $\langle\zeta_n\rangle$ shows a clear increase around $t = 0$ h (the composite time), and the direction of $\langle\zeta_n\rangle$ increases before 0 h and plateaus thereafter (Fig. 7c), indicating a simultaneous increase in vortex tilt magnitude and decrease in precession rate. This behavior can also be seen in the $\langle\zeta_n\rangle$ tendency (Fig. 7b) and the precession rate Ω (Fig. 7d). Near 0 h, $d\langle\zeta_n\rangle/dt$ shows a distinct positive peak, while Ω gradually decreases from positive to negative values. Figures 7b and 7d also show the axial-mean and eddy contributions to $d\langle\zeta_n\rangle/dt$ and Ω. The axial-mean contributions generally have smaller variations, while the eddy contributions are responsible for the larger variations. In Fig. 7b, the strong overlap between the total $d\langle\zeta_n\rangle/dt$ (black line) and the eddy contribution (dashed, blue line) indicates that eddy processes are responsible for the increase in vortex tilt. Looking at the Ω evolution (Fig. 7d), the axial-mean contribution is consistently positive. However, during the hiatus initiation, the axial-mean contribution slightly decreases and is countered by an increasingly negative eddy contribution, leading to the pause of cyclonic precession. This result indicates that the eddy contribution plays an important role in pausing the cyclonic precession during this period.

To identify the regions that contribute the most to the changes near $t = 0$ h, we next examine the vertically

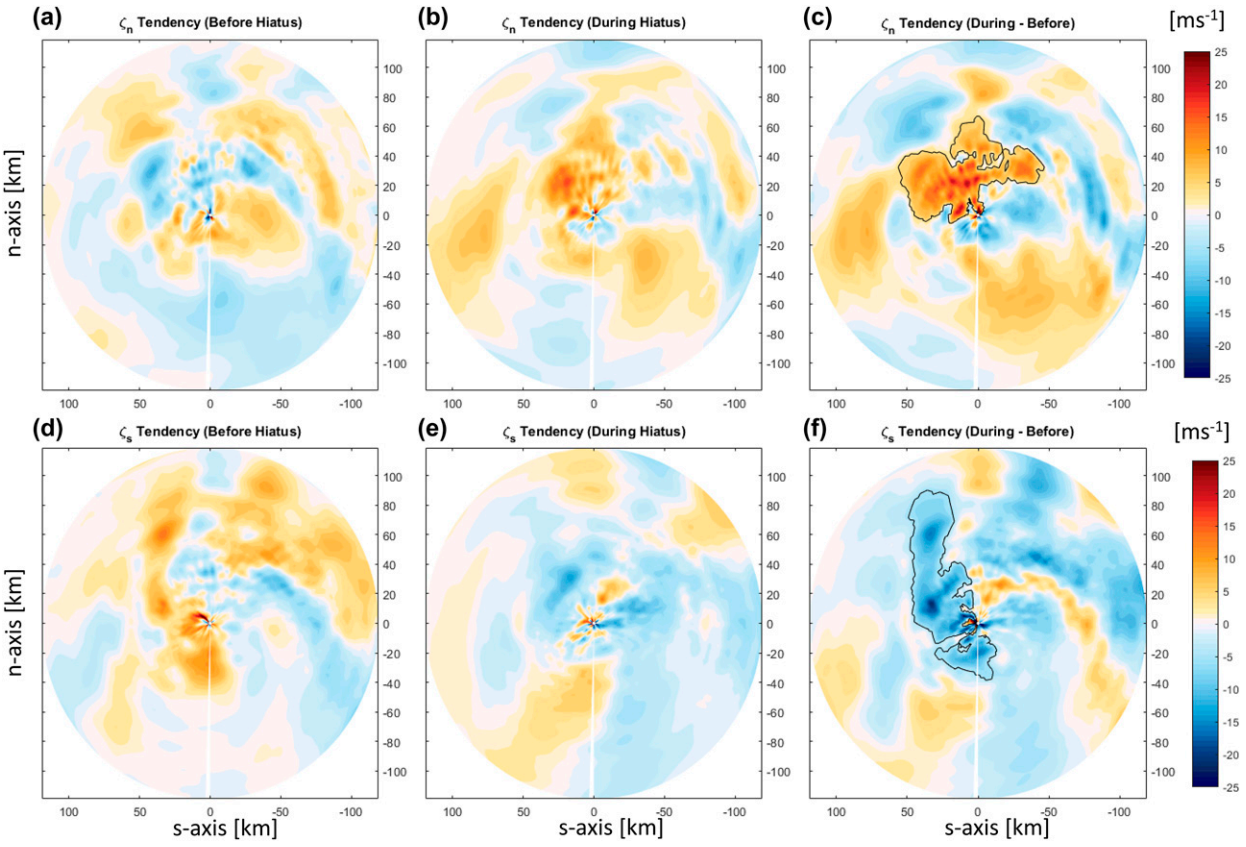

FIG. 8. The vertically integrated ζ_n changes between $z = 1.5$ and 6.5 km, temporally integrated over (a) $t = -5$ to -2.5 h before $\langle\zeta_n\rangle$ increases, (b) $t = -2$ to 0.5 h during the $\langle\zeta_n\rangle$ increase, and (c) the difference between (b) and (a). (d),(e) As in (a) and (b), but for the vertically integrated ζ_s changes during $t = -4.25$ to -1.75 h and 0.5 to 3 h. (f) The difference between (e) and (d). The black contour in (c) indicates the downtilt-left region of interest that has a ζ_n increase greater than 6.5 m s^{-1}. The black contour in (f) indicates the downtilt-left region of interest that has a ζ_s decrease less than -6.5 m s^{-1}.

integrated ζ_n tendency in the rotated $(\hat{\mathbf{n}}, \hat{\mathbf{s}})$ coordinate framework, averaging the tendency across the experiments relative to the midlevel centroids. Figures 8a and 8b show the vertically integrated ζ_n tendency, temporally integrated over the period before (-5 to -2.5 h) and during the precession hiatus (-2 to 0.5 h). The tendency difference between these two periods is shown in Fig. 8c. During -5 to -2.5 h, the ζ_n tendency is generally weak and of varying sign, consistent with the small net tendency shown in Fig. 7b. During -2 to 0.5 h, a distinct region of positive ζ_n tendency emerges in the downtilt-left region, which is more apparent in the difference of the ζ_n tendency between these two periods (Fig. 8c).

Figures 8d and 8e show a similar plot for the vertically integrated ζ_s tendency, which contributes directly to the precession rate Ω of the $\langle\boldsymbol{\zeta}_h\rangle$ vector. In contrast with the ζ_n tendency, during -4.25 to -1.75 h, the ζ_s tendency shows coherent, positive areas in the downtilt region (Fig. 8d). However, when the precession hiatus occurs, these positive areas disappear (Fig. 8e). In particular, the downtilt-left region has the largest negative change (Fig. 8f).

c. *Horizontal vorticity budget in the downtilt-left region*

To understand the increase in vortex tilt and decrease in precession rate during the precession hiatus, we next examine the ζ_n and ζ_s budget terms to quantify the processes that contribute to the $\langle\zeta_n\rangle$ and Ω changes. As shown in Figs. 8c and 8f, the largest changes in both ζ_n and ζ_s occur in the downtilt-left quadrant, which indicate that the dynamical processes in this region are important for the onset of the precession hiatus. To examine the ζ_n and ζ_s budgets more surgically in that region, we average the budget terms over a local, contiguous region that is enclosed by the 6.5 m s^{-1} ζ_n change contour in Fig. 8c and -6.5 m s^{-1} ζ_s change contour in Fig. 8f.

Figures 9a and 9b show the time series of total ζ_n tendency, the axial-mean and eddy components, and the individual eddy terms, averaged over the contoured region in Fig. 8c. From Fig. 9a, we see that the total ζ_n tendency in this region has a positive peak around -2 h when the hiatus occurs, consistent with the peak in the $\langle\zeta_n\rangle$ tendency shown in Fig. 7b. This consistency justifies isolating the analysis to this local, downtilt-left region. The eddy contribution is largely responsible, also consistent with Fig. 7b. To further analyze the eddy

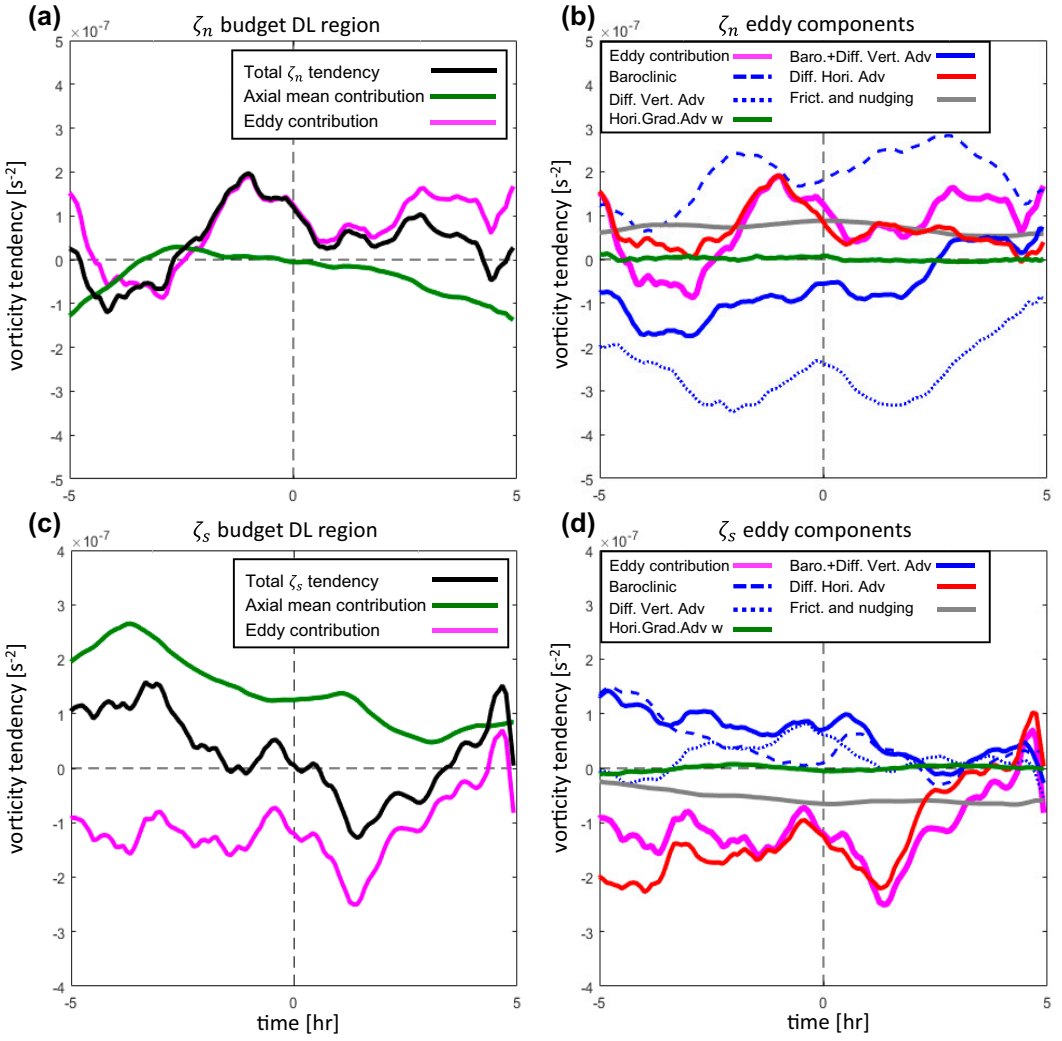

FIG. 9. Time series of the horizontal vorticity budget terms in the downtilt-left regions outlined in Figs. 8c and 8f: (a) area-averaged ζ_n tendency (black), together with the eddy contribution (magenta) and axial-mean contribution (green); (b) decomposition of the eddy contribution with terms given in the legend and described in the text. (c),(d) As in (a) and (b), but for the area-averaged ζ_s tendency.

contribution, Fig. 9b shows the individual terms in (12) that make up the eddy contribution. Since the differential vertical advection and baroclinic term tend to strongly cancel, their sum is also shown in Fig. 9b. From the decomposition, the differential horizontal advection term largely captures the evolution of the total eddy contribution, especially around the peak.

For the slowing of the cyclonic precession, Figs. 9c and 9d show a similar analysis of the ζ_s tendency, averaged over the contoured region in Fig. 8f. As shown in Fig. 9c, the ζ_s tendency in this region decreases starting at -3 h and then reverses sign during 0 to 4 h, consistent with volume-averaged tendency in Fig. 7d. This consistency again justifies isolating the analysis to this local region. The decrease in ζ_s tendency during -3 to 1 h is due to both decreasing axial-mean and eddy contributions. The latter has a greater contribution to this decrease around 0 h, and opposes the positive axial-mean contribution during this period. To further analyze the eddy contribution, Fig. 9d shows the individual terms in (13) that make up the eddy contribution. The decomposition shows that the differential horizontal advection closely matches the evolution of the eddy contribution, particularly the decrease of the ζ_s tendency after 0 h, while the temporal variations of the other terms are smaller.

In summary, the eddy differential horizontal advection term is the major contribution to both the increase in tilt magnitude ($\langle|\zeta_n|\rangle$) and decrease in precession rate (Ω) during the hiatus period. We will explore this term more in the next subsection.

d. *Interpretation of the differential horizontal advection term and its effect on the vertical vorticity structure*

The results from the ζ_n and ζ_s budgets suggest that the differential horizontal advection term plays an important role in

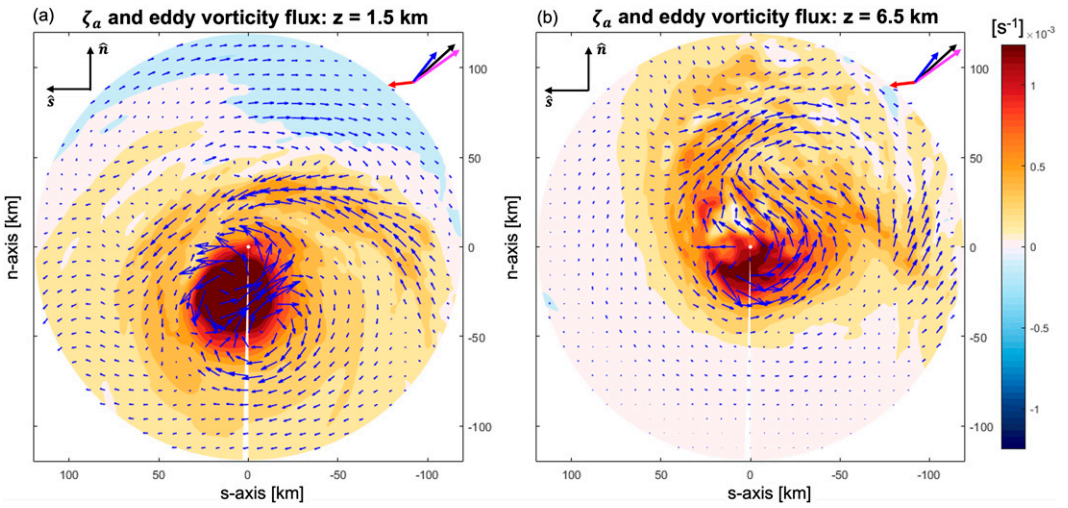

FIG. 10. The composite-mean, vertical component of the absolute vorticity (shaded) during $t = -1.5$ to 2.5 h at (a) $z = 1.5$ km and (b) $z = 6.5$ km. The blue vectors show the eddy vorticity flux. The black arrows at the upper-right corner show the wind shear direction, the red arrows show the average vorticity flux at $z = 1.5$ km, the blue arrows show the average vorticity flux at $z = 6.5$ km, and the magenta arrows show the vorticity flux vector difference between these two levels.

initiating the precession hiatus. Therefore, it is important to understand what this term represents and how it influences the vertical vorticity structure.

Combining the $\hat{\mathbf{n}}$ and $\hat{\mathbf{s}}$ components of differential horizontal advection in (12) and (13) results in

$$\hat{\mathbf{k}} \times \left\langle \frac{\partial}{\partial z}(-\mathbf{v}_h \cdot \nabla_h \mathbf{v}_h) \right\rangle_e . \tag{14}$$

This term represents the generation of horizontal vorticity (and shear) by the vertical difference in the horizontal momentum advection. Using a vector identity, (14) may be rewritten as

$$\hat{\mathbf{k}} \times \left\langle \frac{\partial}{\partial z}(-\mathbf{v}_h \cdot \nabla_h \mathbf{v}_h) \right\rangle_e = \hat{\mathbf{k}} \times \left\langle \frac{\partial}{\partial z}\left(-\frac{1}{2}\nabla_h |\mathbf{v}_h|^2 + \mathbf{v}_h \times \boldsymbol{\zeta}_z \right) \right\rangle_e , \tag{15}$$

where $\boldsymbol{\zeta}_z$ is the vertical vorticity vector.

How does the term in parentheses affect the vertical vorticity structure? The first term inside the parentheses is of the form $\nabla\phi$ and must be irrotational (zero curl), i.e., $\hat{\mathbf{k}} \cdot \nabla_h \times [-(1/2)\nabla_h |\mathbf{v}_h|^2] \equiv 0$, indicating that this term only reflects changes in divergence structure, but not changes in ζ_z structure. Rather, the differential horizontal advection influences the ζ_z structure only through the second term, that is $\hat{\mathbf{k}} \cdot \nabla_h \times [(\partial/\partial z)(\mathbf{v}_h \times \boldsymbol{\zeta}_z)] = -(\partial/\partial z)(\nabla_h \cdot \mathbf{v}_h \zeta_z)$, which is the differential vorticity flux convergence.

Meanwhile, the horizontal vorticity generated by this second term is also associated with the vorticity flux,

$$\hat{\mathbf{k}} \times \left\langle \frac{\partial}{\partial z}(\mathbf{v}_h \times \boldsymbol{\zeta}_z) \right\rangle_e = \left\langle \frac{\partial}{\partial z}(\mathbf{v}_h \zeta_z) \right\rangle_e , \tag{16}$$

We have verified (not shown) that this second term $\langle (\partial/\partial z)(\mathbf{v}_h \zeta_z) \rangle_e$ is dominant on the rhs of (15).

Synthesizing, the differential horizontal advection term influences the ζ_z structure by causing a vertical gradient in vorticity flux convergence, resulting in a change in vortex tilt. As the upper- and lower-level vorticity centroids are pushed farther apart (along the $\hat{\mathbf{n}}$ direction), the differential changes in the (nondivergent) wind field simultaneously generates horizontal vorticity pointing in the $\hat{\mathbf{n}}$ direction, resulting in a positive change in ζ_n. If the differential advection pushes the upper- and lower-level vorticity centroids farther apart in the -$\hat{\mathbf{s}}$ direction (decrease in precession rate Ω), the differential changes in the (nondivergent) wind field also cause a decrease in ζ_s.

We can now apply this differential vorticity flux reasoning to the simulations to diagnose the increase in tilt and decrease in precession rate. Figure 10 shows the composite average absolute vorticity and the eddy vorticity flux at $z = 1.5$ and 6.5 km averaged between −1.5 and 2.5 h. At 1.5 km, eddy vorticity flux near the vorticity center and in the downtilt rainband region predominantly points toward the left-of-tilt direction, resulting in an area-averaged vorticity flux vector that points at the same direction, as shown by the red arrow at the upper-right corner of Fig. 10a. At 6.5 km, positive vorticity anomalies concentrate in the downtilt-left quadrant (Fig. 10b). The location of this downtilt-left vorticity anomaly coincides with the region that exhibits the largest changes in horizontal vorticity tendencies during the hiatus period, shown in Figs. 8c and 8f. In this region, the eddy vorticity flux vectors associated with the vorticity anomaly point toward the positive $\hat{\mathbf{n}}$ and negative $\hat{\mathbf{s}}$ directions, resulting in a mean midlevel vorticity flux vector pointing downtilt-right (blue arrow at the upper-right corner). The resulting differential vorticity flux between mid and low levels also points downtilt-right, as shown by the magenta arrow.

Now, we examine the influence of the differential vorticity flux *convergence* on the vertical vorticity structure. Figure 11a shows that the midlevel eddy vorticity flux in the downtilt-left

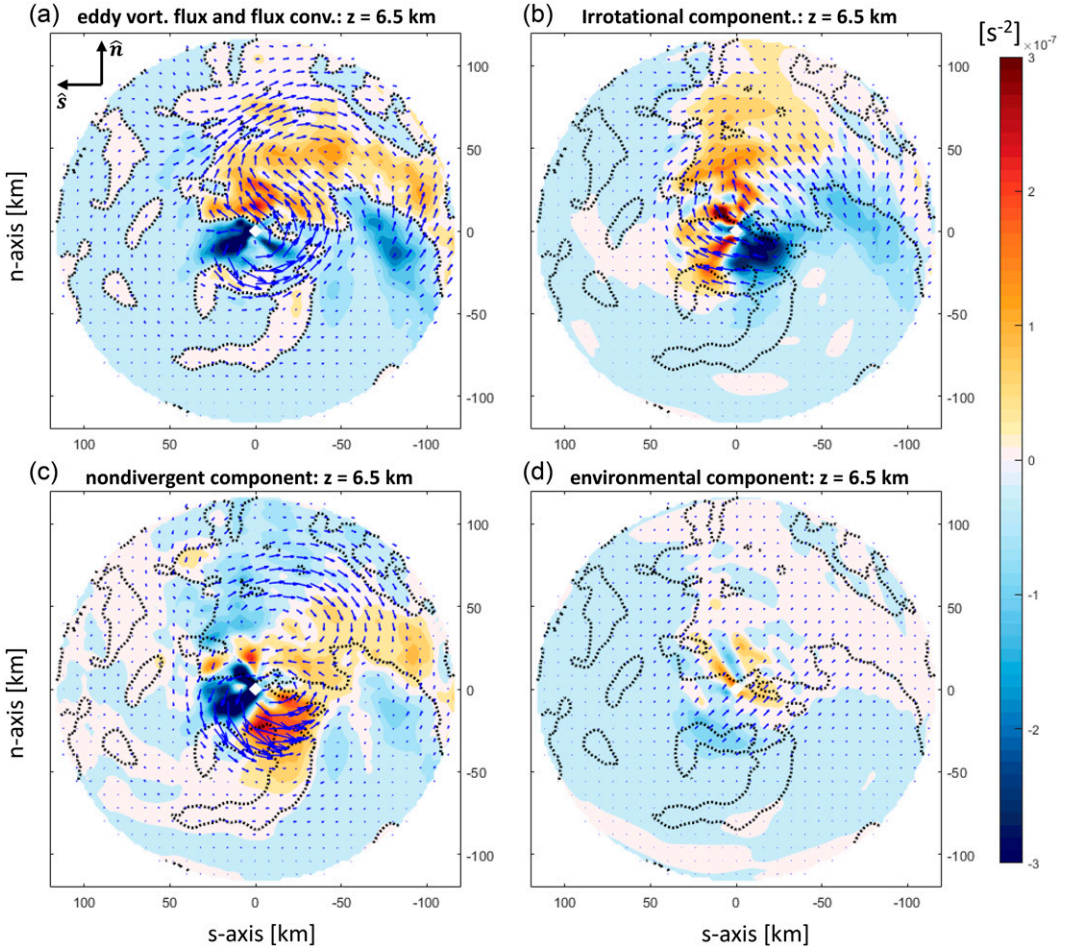

FIG. 11. (a) The composite-mean, eddy vorticity flux (arrows) and flux convergence (shaded; positive is convergence) during $t = -1.5$ to 2.5 h at $z = 6.5$ km. (b)–(d) As in (a), but for the irrotational, nondivergent, and environmental wind components, respectively.

quadrant results in a large area of flux convergence over the downtilt and downtilt-right regions. This convergence results in an enhancement of the midlevel vertical vorticity downtilt and downtilt-right, which simultaneously increases the vortex tilt and decreases the precession rate.

To further investigate how this midlevel eddy vorticity flux comes about, we decompose the flux into the nondivergent ($\mathbf{v}_\psi$), irrotational ($\mathbf{v}_\chi$) and environmental ($\mathbf{v}_{\rm env}$) components:

$$\langle \mathbf{v}_h \zeta_z \rangle_e = \langle \mathbf{v}_\psi \zeta_z \rangle_e + \langle \mathbf{v}_\chi \zeta_z \rangle_e + \langle \mathbf{v}_{\rm env} \zeta_z \rangle_e. \tag{17}$$

Here, the environmental wind is comprised of the prescribed sheared wind profile ($\mathbf{v}_n$) and the storm movement ($\mathbf{v}_c$), i.e., $\mathbf{v}_{\rm env} = \mathbf{v}_n - \mathbf{v}_c$. Then, the wind field is decomposed by first solving for $\mathbf{v}_\chi$ using the free-space Green's function approach (Vico et al. 2016), and $\mathbf{v}_\psi$ is computed as a residual.

Applying this decomposition (Fig. 11), the irrotational component of the vorticity flux $\langle \mathbf{v}_\chi \zeta_z \rangle_e$ (Fig. 11b) provides the largest contribution to the downtilt-pointing eddy vorticity flux and flux convergence (Fig. 11a). The eddy flux convergence of the irrotational component is responsible for the generation of the midlevel positive vorticity anomaly seen in Fig. 10b, and leads to the increase in vortex tilt during the hiatus. In contrast, the nondivergent component (Fig. 11c) contributes to the anticyclonic eddy vorticity flux downtilt and downtilt-right from the midlevel center. This anticyclonic vorticity flux has flux divergence downtilt (Fig. 11c), partially offsetting the flux convergence of the irrotational component, and flux convergence downtilt-right. This pattern indicates that the nondivergent component moves the midlevel vorticity generated in the downtilt region toward the downtilt-right, contributing to the decrease in precession rate. On the other hand, the direct contribution of the environmental component to eddy vorticity flux is small (Fig. 11d). However, the environmental wind shear plays an essential role in maintaining the downtilt convection, displacing hydrometeors further downtilt and influencing the location of stratiform precipitation, so indirectly contributes to the irrotational flux component.

We conducted additional experiments turning the large-scale nudging (shear) off at various times (2, 5, and 11 h)

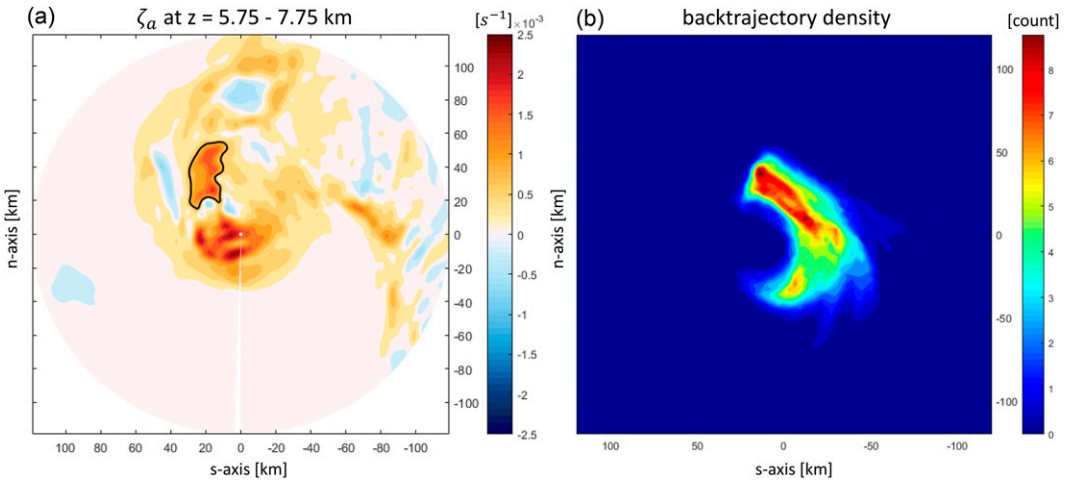

FIG. 12. (a) The vertically averaged absolute vorticity ζ_a during $t = -1$ to 0 h for the CTRL experiment. The black contour shows region where back-trajectory calculations are initialized between 5.75 and 7.75 km within $\zeta_a > 8 \times 10^{-4}\,\mathrm{s}^{-1}$. (b) The back-trajectory density, computed by summing the normalized parcel distribution (normalized by the peak value) at 5-min intervals.

before the onset of precession hiatus. In these experiments, the precession hiatus does not occur, confirming the role of environmental wind shear in indirectly modulating the eddy vorticity flux and flux convergence patterns (not shown). The diabatic processes and rainband features associated with the midlevel eddy vorticity flux will be investigated in more detail in the next section.

5. Vertical vorticity budget

The previous horizontal vorticity budget analysis shows that the differential horizontal vorticity flux and vorticity flux convergence in the downtilt region plays an essential role in causing the increase in the vortex tilt and the pause in cyclonic precession. This differential vorticity flux is associated with the emergence of a coherent, positive midlevel vorticity anomaly in the downtilt-left quadrant. Given the importance of this vorticity anomaly, we now perform an absolute vertical vorticity budget in a Lagrangian framework to understand how this feature is generated. In a Lagrangian framework, the absolute vorticity equation is

$$\frac{D\zeta_a}{Dt} = -\zeta_a \nabla_h \cdot \mathbf{v}_h + \boldsymbol{\zeta}_h \cdot \nabla_h w + \hat{\mathbf{k}} \cdot \nabla p \times \nabla \alpha + \hat{\mathbf{k}} \cdot \nabla \times \mathbf{F}. \tag{18}$$

The terms on the rhs of (18) are the stretching, tilting, baroclinic, and frictional torque terms.

The Lagrangian calculation is performed using the Lagrangian Analysis Tool (LAGRANTO; Wernli and Davies 1997; Sprenger and Wernli 2015). Backward trajectories are calculated using 5-min model output. To focus on the positive vorticity anomaly in the downtilt-left quadrant, we initialize back trajectories within the contoured region in Fig. 12a between $z = 5.75$ and 7.75 km, spanning -1 to 0 h with parcels seeded every five minutes. Due to the large number of trajectories, we will only focus on the CTRL experiment, as the other experiments have a similar interpretation. The back trajectory density (Fig. 12b) shows air parcels originating in the uptilt region and circulating cyclonically before comprising the downtilt-left, positive vorticity anomaly.

Figure 13a shows that these parcels ascended and increased in vorticity. Figure 13b shows that stretching is the dominant process in enhancing the vorticity from -70 to -40 min during the ascent right of tilt. The right-of-tilt ascent may be due to ascent along slanted isentropes (Jones 1995; Boehm and Bell 2021) and/or driven by boundary layer convergence (Schecter 2022). This period of ascent is followed by a period (-40 to -20 min) when tilting becomes dominant. Importantly, parcel vorticity exhibits a sharp increase during -20 to 0 min, which is primarily caused by vertical vorticity stretching. The magnitude of the stretching is large, despite the parcel ascent decreasing during this period (flattening of red line in Fig. 13a). These results indicate that strong vortex stretching above 6 km is important for boosting the positive vorticity anomaly in the downtilt-left region shown in Fig. 12a.

Figure 14 examines the spatial structure of contributions to the positive vorticity anomaly in the downtilt-left region. Here, there is a band of positive vorticity stretching (Fig. 14a). To assess the precipitation structures associated with this vorticity stretching, a precipitation classification algorithm, based on surface precipitation rate (Braun et al. 2010), is applied to classify the precipitation into convective or stratiform (Fig. 14a). Regions with positive midlevel stretching almost entirely reside in the stratiform precipitation region at the immediate outward side of the convective precipitation in the downtilt-left quadrant.

To investigate the mesoscale features responsible for the midlevel vertical vorticity stretching, accounting for its curved shape, we construct cross sections centered along a spiral that passes through the local maxima of vertically averaged vorticity stretching. This central spiral is defined using cubic splines

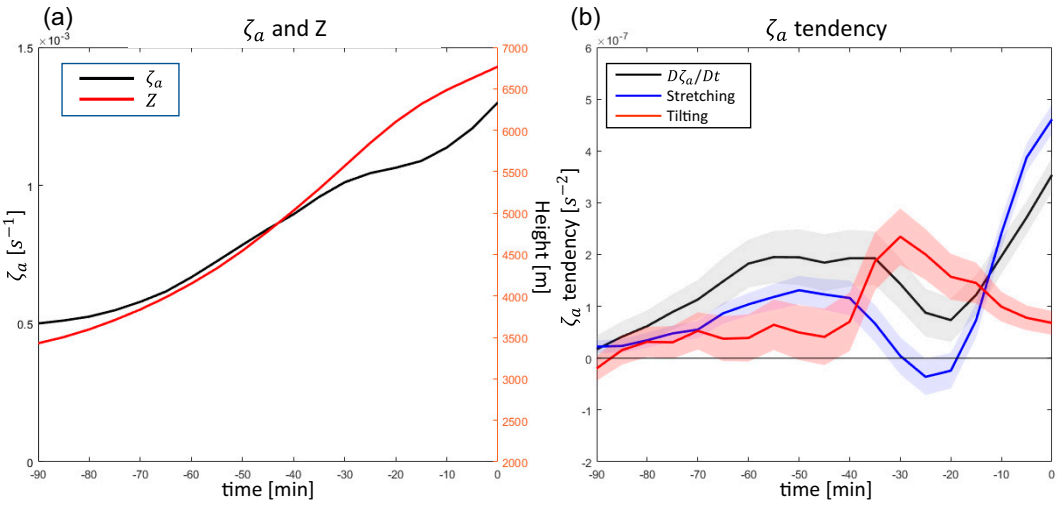

FIG. 13. (a) The mean absolute vorticity and height along back trajectories and (b) the Lagrangian change in absolute vorticity and the contribution from stretching and tilting. The frictional and baroclinic effects are negligible and not shown. The shading in (b) shows one standard deviation from the mean.

on four subjectively determined anchor points, as shown by the green dots and blue solid curve in Fig. 14a. After this central spiral is defined, radial–height cross sections are constructed at each azimuth centered along the axis of the spiral, covering a radial distance of 35 km relative to the spiral (Fig. 14a). Then, an azimuthal average is performed to produce an average cross section along the spiral.

Between $z = 5$ and 8 km, a layer of positive vorticity stretching occurs between an upper-level updraft and lower-level downdraft (Fig. 14b). This vertical velocity structure is driven by diabatic heating and cooling above and below the melting level (Fig. 14c), which is associated with the stratiform precipitation region of the principal rainband, consistent with the precipitation classification shown in Fig. 14a.

The positive vorticity anomalies generated via stretching are advected outward by radial outflow (Fig. 14c), constituting a midlevel outward flux of absolute vorticity that points toward the downtilt-right direction at larger radii, as shown in Fig. 10b. Recall from Fig. 11b that the irrotational wind at $z = 6.5$ km provides a major contribution of the eddy vorticity flux and vorticity flux convergence in the downtilt region. As shown in Fig. 14d, the irrotational wind between $z = 5$ and 8 km is the major component of the radial outflow (green arrow). This irrotational outflow is driven by divergence associated with inner convective precipitation (blue box) and convergence associated with outer stratiform precipitation (red box). This dipole of inner divergence and outer convergence is due to the transition from bottom-heavy to top-heavy diabatic heating profiles of the downtilt convective and stratiform regions. Therefore, the downtilt irrotational component of the eddy vorticity flux and vorticity flux convergence (Fig. 11b) is a product of the irrotational outflow driven by the inner convective to outer stratiform diabatic process, coupled with midlevel vorticity generation due to stretching within the stratiform region.

Meanwhile, the cooling-driven downdraft below $z = 5$ km also causes vortex compression (negative stretching), which results in a negative vorticity anomaly at low levels (Fig. 14c). As we illustrated in the schematic diagram in Fig. 3a, the development of the positive vorticity anomaly aloft and the negative vorticity anomaly beneath enhances the vorticity perturbation associated with the tilted structure of the vortex, consistent with Reasor and Montgomery (2001) and Davis et al. (2008). In addition, the cooling-driven downdraft has a clear inflow component (Figs. 14c,d) below 3 km, which resembles mesoscale descending inflow (Didlake and Houze 2013). Alland et al. (2021a) showed that environmental dry air can strengthen the cooling-driven downdraft, resulting in more low-θ_E air being flushed into the boundary layer. Additionally, from Fig. 14a, the uptilt side of storm is mostly free of convection, which is due to the combined effect of adiabatic descent associated with the tilted vortex and the environmental dry air wrapping inward, similar to that noted in Alland et al. (2021b). These thermodynamic effects will be examined in a subsequent study.

6. Conclusions

This study investigated the dynamics leading to the initiation of a vortex precession hiatus when a tropical cyclone is under the influence of vertical wind shear of a critical magnitude. For our model configuration in which the initial RH above 850 hPa is 50%, this critical wind shear is 7.5 m s^{-1}. The critical shear value for a moister environment could be larger. The hiatus is characterized by a pause in precession and an increase in tilt magnitude toward the downshear-left quadrant. To examine the hiatus dependence on the TC vorticity structure near this critical shear regime, a balanced perturbation method is used to enhance the mid- to upper-level, inner-core vorticity by various percentages. The simulation results show that the precession hiatus leads to diverging tilt

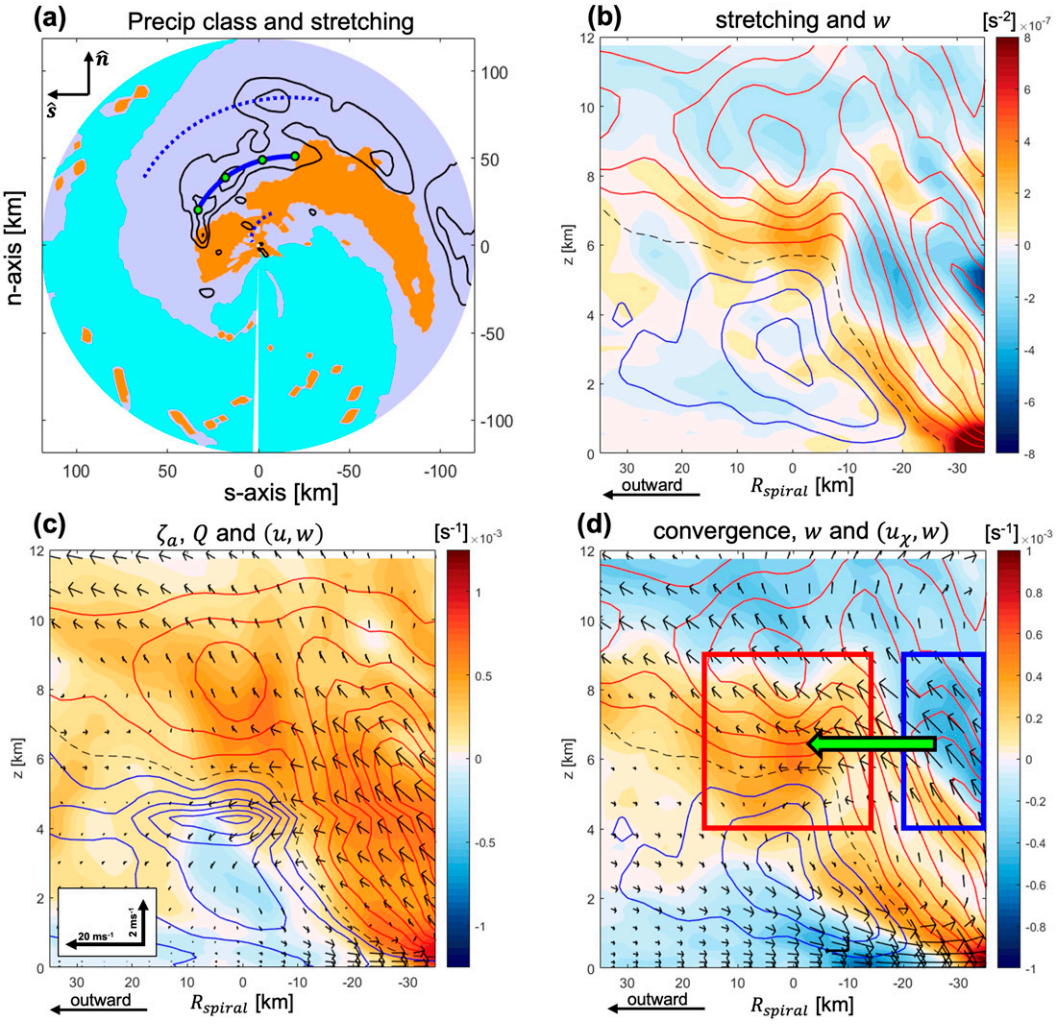

FIG. 14. (a) Plan view of precipitation classification for the CTRL experiment for time period between −1.5 and 1.5 h. Orange denotes convective precipitation, purple denotes stratiform precipitation, and cyan notes nonprecipitating region. The positive vortex stretching, averaged between 5.25 and 8 km, is shown in black contours at every 5×10^{-7} s^{-2}. The blue solid curve and green dots define the central spiral used in calculating the cross sections. The dotted curves show the radial bounds of the cross section. (b) Cross section of vorticity stretching (shading) and vertical velocity (updrafts in red and downdrafts in blue, every 0.2 m s^{-1}; zero line dashed). (c) Cross section of absolute vorticity (shading), diabatic tendencies (heating in red, contoured at every 10^{-3} K s^{-1}; cooling in blue, contoured at every 5×10^{-4} K s^{-1}; zero line dashed), and wind in the plane of the cross section (vectors). (d) As in (c), but for convergence (shading), vertical velocity (contours), and irrotational wind in the plane of the cross section (vectors). The blue and red boxes indicate regions of divergence and convergence mentioned in the text; the green arrow highlights midlevel outward pointing irrotational wind. The black arrow at the bottom left of (b)–(d) indicate the spiral-relative outward direction.

and intensification evolutions depending on whether the TC is able to recover from the hiatus. Of specific interest in this study, the precession hiatus occurred in all the simulations.

To examine the dynamics that lead to the initiation of the precession hiatus and increase in vortex tilt, we examine the budgets of the volume-averaged horizontal vorticity vector $\langle \boldsymbol{\zeta}_h \rangle$. We showed that a nonzero $\langle \boldsymbol{\zeta}_h \rangle$ is physically linked to the vortex tilt. During the hiatus period, $\langle \boldsymbol{\zeta}_h \rangle$ shows a substantial increase in magnitude and a decrease in the precession rate Ω, consistent with the vortex tilt vector. Examination of the horizontal vorticity budgets shows that the increase in the $\langle \boldsymbol{\zeta}_h \rangle$ magnitude is largely the result of positive ζ_n generation in the downtilt-left region. Simultaneously, this region also has production of negative ζ_s, leading to a decrease in the precession rate. The budgets of ζ_n and Ω suggest that the increase in horizontal vorticity (and vortex tilt) and pause in precession are due to an increasing eddy vorticity flux that points toward the downtilt-right quadrant at midlevels.

Figure 15 shows an illustration of processes and corresponding regions that contribute to the midlevel eddy vorticity flux.

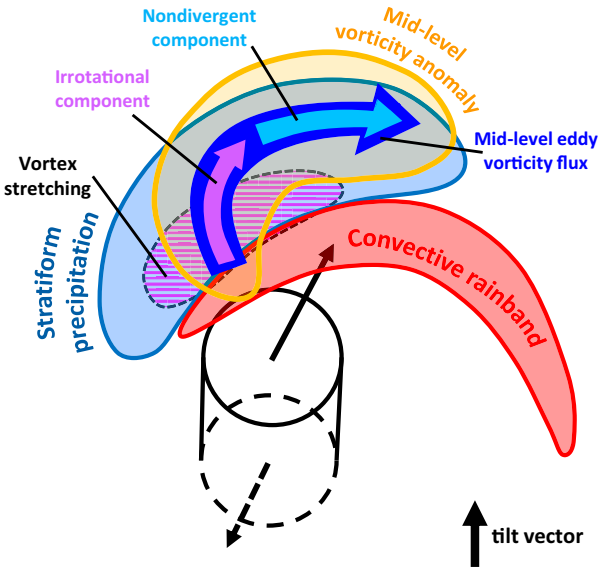

FIG. 15. (a) Summary schematic of relevant processes causing the precession hiatus in the simulations. The vortex tilt (cylinder) is pointing north. The red region indicates the convective portion of the principal rainband, and the blue region indicates the stratiform portion of the rainband. The striped region indicates the region of midlevel vortex stretching. The orange shaded region represents the coherent midlevel vorticity anomaly. The blue, curved arrow indicates the outward flux of positive eddy vorticity associated with the enhanced midlevel vorticity anomaly, which consists of irrotational component at the inner region (purple curved arrow) and nondivergent component at the outer region (light-blue curved arrow). The storm-relative environmental wind at the upper (lower) levels is shown by the solid (dashed) black arrow.

These processes occur in the downtilt region where the rainband precipitation transitions from a convective to stratiform structure. Ascent above 6 km and descent below 6 km within the stratiform region, characteristic of the stratiform rainband structure (Didlake and Houze 2013), cause strong vortex stretching. In the downtilt-left quadrant, this vortex stretching enhances a coherent midlevel positive vorticity anomaly and the subsequent increase in the midlevel eddy vertical vorticity flux. Further decomposition of the midlevel eddy vorticity flux shows that the irrotational component is responsible for the eddy vorticity flux convergence downtilt, increasing the midlevel, positive vorticity anomaly further downtilt and, thus, the vortex tilt. The nondivergent component of eddy vorticity flux then displaces the downtilt vorticity toward the downtilt-right, slowing down the vortex precession. Meanwhile, the descent below 6 km is associated with negative vortex stretching (vortex compression), resulting in negative vorticity anomalies at lower levels. The resulting vertical dipole of vorticity anomalies in the downtilt-left region enhances the tilted vortex structure and reinforces the differential vorticity flux that causes the precession hiatus.

While the direct contribution of the environmental wind (shear) to the eddy vorticity flux is small, the shear is important for indirectly contributing to the eddy vorticity flux structure. The shear sustains the asymmetric, downtilt convection and helps to maintain the convective-to-stratiform transition zone in the downtilt-left quadrant.

What is the context of these results relative to previous studies on TC tilt and precession? First, the downshear-left equilibrium configuration has been demonstrated in dry, vertically sheared TC-like vortices in previous work (e.g., Reasor et al. 2004). Our findings indicate that the quasi-stationary tilt configuration in our simulations is the result of the interaction between vertical wind shear and the concurrent vortex dynamics associated with both convective and stratiform diabatic processes. Second, Schecter (2022) showed that, in the context of shear-free dynamics, nonmonotonic growth of vortex tilt may be caused by an organized negative vorticity region in the convective rainband region, which advects the upper-level vortex away from the low-level center. However, in a steady-shear environment near the critical regime, the working mechanism of the precession hiatus found in our study seems to be different. Third, previous studies showed that the spinup of midlevel vortex may be important for the early stage TC development and tropical cyclogenesis (Raymond et al. 2014; Gjorgjievska and Raymond 2014). Our results suggest that near the critical shear regime, the downtilt development of a midlevel vortex aided by stratiform precipitation could in turn inhibit realignment and intensification, particularly in a drier environment, like the one in our simulations.

While the focus of our study is to examine the dynamical process that initiates the precession hiatus, the left-of-tilt stratiform precipitation region also imposes thermodynamic impacts on the TC intensity during the hiatus initiation period. Prior studies have shown downdraft ventilation flushes low-θ_E air into the boundary layer (from both convective and stratiform precipitation), hindering TC intensification (Riemer et al. 2010, 2013; Riemer and Montgomery 2011; Tang and Emanuel 2010, 2012a,b; Alland et al. 2021a,b). Conversely, the saturated downdraft in the stratiform region could also help to moisten lower levels (Alvey et al. 2020), contributing to a favorable thermodynamic environment for new convection after sufficient boundary layer recovery. Exactly how these two competing thermodynamic effects combine with the negative dynamical impact identified in this study to result in the diverging behaviors of our simulations after the precession hiatus in the critical shear regime will be the subject of a follow-on study.

The precession hiatus behavior examined in this study occurs at a critical shear regime specific to our simulation design. The shear magnitude of this critical regime likely varies as a function of both the TC environment and initial vortex structure, such as environment and inner-core moisture distribution, sea surface temperature, the initial vortex structure, etc. Other TC behavior in shear, such as downshear reformation and vortex repositioning, was not captured in the current experiment design. Given the sensitivity of TC intensity evolution in this critical shear regime, identifying how this critical shear regime varies as a function of these parameters, and influences the tilted TC vortex structure evolution, would also be of value.

Acknowledgments. We thank George Bryan, Jun Zhang, Falko Judt, Rosimar Rios-Berrios, and Kristen Corbosiero

for their thoughtful comments on this study. We also thank the anonymous reviewers whose comments led to significant improvements in the manuscript. This research was supported by the Office of Naval Research Grant N000142012071.

Data availability statement. The CM1 namelist files and model output are available upon request via a University at Albany Thematic Real-time Environmental Distributed Data Services (THREDDS) server.

APPENDIX A

Balanced Perturbation Method

In this appendix, we document the strategy used to insert a balanced vorticity perturbation into our simulations. The goal of this approach is to derive the responses in the mass and thermodynamic fields such that a vorticity perturbation can be added to a simulation without disturbing the unbalanced flow present in the original flow.

As introduced in section 2c, this approach relies on the NLBE and hydrostatic balance, as discussed in Eqs. (2) and (3). The NLBE equation is derived from the divergence equation:

$$\begin{aligned}\frac{\partial \delta}{\partial t} &+ \nabla\cdot[(\mathbf{v}_\psi\cdot\nabla)\mathbf{v}_\chi + (\mathbf{v}_\chi\cdot\nabla)\mathbf{v}_\psi + (\mathbf{v}_\chi\cdot\nabla)\mathbf{v}_\chi] \\ &+ \nabla\cdot\left(w\frac{\partial \mathbf{v}}{\partial z}\right) + \nabla\cdot[(\mathbf{v}_\psi\cdot\nabla)\mathbf{v}_\psi] \\ &= -\nabla\cdot(c_p\theta_\rho\nabla\pi) + f\nabla^2\psi + \nabla\cdot\mathbf{F}, \end{aligned} \tag{A1}$$

where $\delta = \nabla\cdot\mathbf{v}$ is the horizontal divergence, $\mathbf{v}_\chi = -\nabla\chi$ is the irrotational wind with χ being the velocity potential, $\mathbf{v}_\psi = \hat{\mathbf{k}}\times\nabla\psi$ is the nondivergent wind with ψ being the streamfunction, and $\mathbf{F}$ is friction. The NLBE is obtained by neglecting the divergence tendency, the advection terms involving $\mathbf{v}_\chi$ and w, and the divergence of momentum forcing. In general, these terms may not be negligible. We may group these terms as a residual term Res. Expanding $\nabla\cdot[(\mathbf{v}_\psi\cdot\nabla)\mathbf{v}_\psi] = 2[-\psi_{xx}\psi_{yy} + (\psi_{xy})^2]$, Eq. (A1) then becomes

$$\nabla\cdot(c_p\theta_{\rho1}\nabla\pi_1) = 2[\psi_{1xx}\psi_{1yy} - (\psi_{1xy})^2] + f\nabla^2\psi_1 + \mathrm{Res}_1, \tag{A2}$$

where $\mathrm{Res}_1 = -(\partial\delta/\partial t) - \nabla\cdot[(\mathbf{v}_{\psi_1}\cdot\nabla)\mathbf{v}_\chi + (\mathbf{v}_\chi\cdot\nabla)\mathbf{v}_{\psi_1} + (\mathbf{v}_\chi\cdot\nabla)\mathbf{v}_\chi] - \nabla\cdot[w(\partial\mathbf{v}_\chi/\partial z) + w(\partial\mathbf{v}_{\psi_1}/\partial z)] + \nabla\cdot\mathbf{F}$. Here, the additional subscript "1" denotes the original flow fields before the vorticity perturbation is introduced. Similarly, for the flow after the perturbation is introduced, the horizontal balance can be written as

$$\nabla\cdot(c_p\theta_{\rho2}\nabla\pi_2) = 2[\psi_{2xx}\psi_{2yy} - (\psi_{2xy})^2] + f\nabla^2\psi_2 + \mathrm{Res}_2, \tag{A3}$$

where $\mathrm{Res}_2 = -(\partial\delta/\partial t) - \nabla\cdot[(\mathbf{v}_{\psi_2}\cdot\nabla)\mathbf{v}_\chi + (\mathbf{v}_\chi\cdot\nabla)\mathbf{v}_{\psi_2} + (\mathbf{v}_\chi\cdot\nabla)\mathbf{v}_\chi] - \nabla\cdot[w(\partial\mathbf{v}_\chi/\partial z) + w(\partial\mathbf{v}_{\psi_2}/\partial z)] + \nabla\cdot\mathbf{F}$. The subscript "2" denotes the flow fields after vorticity perturbation is introduced. By writing the responses of all variables as q', i.e., $q_2 = q_1 + q'$ (q can be π, θ_ρ, $\mathbf{v}_\psi$ or ψ), Res_2 may be expressed as

$$\mathrm{Res}_2 = \mathrm{Res}_1 - \nabla\cdot[(\mathbf{v}'_\psi\cdot\nabla)\mathbf{v}_\chi + (\mathbf{v}_\chi\cdot\nabla)\mathbf{v}'_\psi] - \nabla\cdot\left(w\frac{\partial\mathbf{v}'_\psi}{\partial z}\right). \tag{A4}$$

The second and third terms in the right-hand side of Eq. (A4) reflect the effect of $\mathbf{v}'_\psi$ on the residual term. If the perturbation vorticity is small compared to the original vorticity field, i.e., $|\mathbf{v}'_\psi| \ll |\mathbf{v}_{\psi1}|$, we can drop these terms and assume $\mathrm{Res}_2 \approx \mathrm{Res}_1$. This assumption yields a diagnostic equation between π', θ'_ρ, and ψ' by subtracting Eqs. (A3) and (A2):

$$\begin{aligned}c_p\nabla\cdot\theta_{\rho2}\nabla\pi' + c_p\nabla\cdot\theta'_\rho\nabla\pi_1 = f\nabla^2\psi' + 2(\psi'_{xx}\psi_{1yy} + \psi_{1xx}\psi'_{yy} \\ + \psi'_{xx}\psi'_{yy} - 2\psi'_{xy}\psi_{1xy} - \psi'^2_{xy}).\end{aligned} \tag{A5}$$

Here, ψ' is the streamfunction of a prescribed vorticity perturbation and is therefore given. The same procedure can be applied to the hydrostatic equation to yield

$$\theta'_\rho\left[c_p\frac{\partial(\pi' + \pi_1)}{\partial z} - \frac{g}{\theta_{\rho2}}\right] = -c_p\theta_{\rho1}\frac{\partial\pi'}{\partial z}. \tag{A6}$$

Equations (A5) and (A6) together form an equation system for solving for π' and θ'_ρ for a given perturbation specified through ψ', such that deviations from nonlinear and hydrostatic balance in the original flow are retained.

An iterative procedure is used to solve Eqs. (A5) and (A6) for θ'_ρ and π' within the CM1 domain. In each iteration, Eq. (A5) is first solved with a zero Dirichlet boundary condition ($\pi'|\partial = 0$) to yield an updated π'. This Dirichlet boundary condition is reasonable, because the nondivergent wind perturbation $\mathbf{v}'_\psi$ decays to zero well within the domain. Then, θ'_ρ is calculated given the updated π'. This iterative procedure converges to a solution in about 15 iterations, but 30 iterations are used to be safe.

After obtaining the responses in θ'_ρ and π', an additional decision must be made to partition the response between the potential temperature θ' and mixing ratio q'_v. One possibility is to require the relative humidity remain unchanged after the balanced perturbation is introduced. Then, θ' and q'_v can thus be solved by iterating

$$\theta_{\rho2} = \theta_2\left(\frac{1 + q_{v2}/\varepsilon}{1 + q_{v2} + q_l + q_i}\right), \tag{A7}$$

$$q_{v2} = \mathrm{RH}\times q_{vs}(p_2, \theta_2), \tag{A8}$$

where RH is relative humidity; q_{vs} (p, θ) is saturation vapor pressure, which is a function of pressure and potential temperature; q_l and q_i are the mixing ratios of liquid water and ice. Note that in the above treatment, we also assume any hydrometeors (q_l, q_i) remain unchanged.

APPENDIX B

Vorticity Equations in the Rotating Coordinate

In this appendix, we derive the three-dimensional vorticity budget equations in the rotating coordinate system ($\hat{\mathbf{n}}$, $\hat{\mathbf{s}}$, $\hat{\mathbf{k}}$), where $\hat{\mathbf{n}}$ and $\hat{\mathbf{s}}$ are the unit vector pointing along the directions parallel and perpendicular to the volume averaged horizontal vorticity vector $\langle\boldsymbol{\zeta}_h\rangle$, as defined in section 2e.

Starting with the momentum equation in vector form, we take the cross product:

$$\frac{\partial}{\partial t}(\nabla\times\mathbf{v})-\nabla\times(\mathbf{v}\times\boldsymbol{\zeta})+\nabla\times[f\hat{\mathbf{k}}\times(\mathbf{v}-\mathbf{v}_g)]=-\nabla\times(\alpha\nabla p)+\nabla\times\mathbf{F}, \tag{B1}$$

where $\boldsymbol{\zeta}=\nabla\times\mathbf{v}$ is the relative vorticity, and $\mathbf{v}_g$ is the wind profile used in the large-scale nudging method. Defining the absolute vorticity vector not including the wind shear as $\boldsymbol{\zeta}_a=\nabla\times(\mathbf{v}-\mathbf{v}_g)+f\hat{\mathbf{k}}$ assuming an f plane, noting that $(\partial\nabla\times\mathbf{v}_g)/\partial t=0$ and taking a dot product with $\nabla\phi$ (ϕ is a scalar field),

$$\nabla\phi\cdot\frac{\partial}{\partial t}(\boldsymbol{\zeta}_a)-\nabla\phi\cdot\nabla\times(\mathbf{v}\times\boldsymbol{\zeta})=-\nabla\phi\cdot\nabla\times[f\hat{\mathbf{k}}\times(\mathbf{v}-\mathbf{v}_g)]-\nabla\phi\cdot\nabla\times(\alpha\nabla p)+\nabla\phi\cdot\nabla\times\mathbf{F}. \tag{B2}$$

The second term may be simplified as

$$\nabla\phi\cdot\nabla\times(\mathbf{v}\times\boldsymbol{\zeta})=-\nabla\cdot[\nabla\phi\times(\mathbf{v}\times\boldsymbol{\zeta})]+(\mathbf{v}\times\boldsymbol{\zeta})\cdot\nabla\times\nabla\phi=-\nabla\cdot[\mathbf{v}(\boldsymbol{\zeta}\cdot\nabla\phi)-\boldsymbol{\zeta}(\mathbf{v}\cdot\nabla\phi)]. \tag{B3}$$

First, we consider ϕ to be the displacement along $\hat{\mathbf{n}}$, that is, $\nabla\phi=\hat{\mathbf{n}}$. Equation (B3) becomes

$$\hat{\mathbf{n}}\cdot\nabla\times(\mathbf{v}\times\boldsymbol{\zeta})=-\nabla\cdot[\mathbf{v}(\boldsymbol{\zeta}\cdot\hat{\mathbf{n}})-\boldsymbol{\zeta}(\mathbf{v}\cdot\hat{\mathbf{n}})]=-\nabla\cdot(\mathbf{v}\zeta_n-\boldsymbol{\zeta}v_n)=-\nabla_{s,k}\cdot(\mathbf{v}_{s,k}\zeta_n-\boldsymbol{\zeta}_{s,z}v_n), \tag{B4}$$

where $\nabla_{s,k}=(\partial/\partial s)\hat{\mathbf{s}}+(\partial/\partial z)\hat{\mathbf{k}}$, $\mathbf{v}_{s,k}=v_s\hat{\mathbf{s}}+w\hat{\mathbf{k}}$, and $\boldsymbol{\zeta}_{s,z}=\zeta_s\hat{\mathbf{s}}+\zeta_z\hat{\mathbf{k}}$ are the gradient operator, wind velocity, and absolute vorticity in the vertical plane spanned by $\hat{\mathbf{s}}$ and $\hat{\mathbf{k}}$. Note that the divergence only operates on the plane spanned by $\hat{\mathbf{s}}$ and $\hat{\mathbf{k}}$ since the $\hat{\mathbf{n}}$ components of $\mathbf{v}\zeta_n$ and $\boldsymbol{\zeta}v_n$ cancel. By expanding the vorticity, Eq. (B4) can be written as

$$\hat{\mathbf{n}}\cdot\nabla\times(\mathbf{v}\times\boldsymbol{\zeta})=-\frac{\partial}{\partial z}(-\mathbf{v}_h\cdot\nabla_h v_s)-\frac{\partial}{\partial z}\left(-w\frac{\partial v_s}{\partial z}\right)+\frac{\partial}{\partial s}(-\mathbf{v}\cdot\nabla w).$$

The first two terms represent the differential horizontal and vertical advection of v_s, and the third term represents the differential advection of w along the $\hat{\mathbf{s}}$ direction.

The forcing term due to nudging is

$$-\hat{\mathbf{n}}\cdot\nabla\times[f\hat{\mathbf{k}}\times(\mathbf{v}-\mathbf{v}_g)]=\nabla\cdot\{f\hat{\mathbf{k}}[(\mathbf{v}-\mathbf{v}_g)\cdot\hat{\mathbf{n}}]\}=f\frac{\partial(v_n-v_{gn})}{\partial z}. \tag{B4}$$

Putting all the expressions together, Eq. (B2) becomes

$$\hat{\mathbf{n}}\cdot\frac{\partial}{\partial t}(\boldsymbol{\zeta}_a)=-\frac{\partial}{\partial z}(-\mathbf{v}_h\cdot\nabla_h v_s)-\frac{\partial}{\partial z}\left(-w\frac{\partial v_s}{\partial z}\right)+\frac{\partial}{\partial s}(-\mathbf{v}\cdot\nabla w)+f\frac{\partial(v_n-v_{gn})}{\partial z}+\hat{\mathbf{n}}\cdot\nabla p\times\nabla\alpha+\hat{\mathbf{n}}\cdot\nabla\times\mathbf{F}. \tag{B5}$$

So far, all terms in Eq. (B5) are casted in a nonrotating coordinate. For a rotating coordinate, the local tendency $(\partial/\partial t)(\boldsymbol{\zeta}_a)$ needs to be rewritten in terms of local tendency in a rotating coordinate, denoted by $\partial_\Omega/\partial t$. It can be shown that $(\partial/\partial t)(\boldsymbol{\zeta}_a)$ and $(\partial_\Omega/\partial t)(\boldsymbol{\zeta}_a)$ are related as follows (Holton 1992):

$$\frac{\partial}{\partial t}(\boldsymbol{\zeta}_a)=\frac{\partial_\Omega}{\partial t}(\boldsymbol{\zeta}_a)-[(\Omega\hat{\mathbf{k}}\times\mathbf{r})\cdot\nabla]\boldsymbol{\zeta}_a+\Omega\hat{\mathbf{k}}\times\boldsymbol{\zeta}_a=\frac{\partial_\Omega}{\partial t}(\boldsymbol{\zeta}_a)-\Omega\frac{\partial\boldsymbol{\zeta}_a}{\partial\lambda}+\Omega\hat{\mathbf{k}}\times\boldsymbol{\zeta}_a, \tag{B6}$$

where Ω is the rotation rate of the coordinate, which is the rotation rate of $\langle\boldsymbol{\zeta}_h\rangle$ in our case. The second and third terms of Eq. (B6) are the apparent changes of the vector field $\boldsymbol{\zeta}_a$ due to the rotation of the coordinate system. Taking the dot product with $\hat{\mathbf{n}}$, we have

$$\hat{\mathbf{n}}\cdot\frac{\partial}{\partial t}(\boldsymbol{\zeta}_a)=\frac{\partial_\Omega}{\partial t}(\zeta_n)-\Omega\frac{\partial\zeta_n}{\partial\lambda}-\Omega\zeta_s. \tag{B7}$$

Then, Eq. (B5) becomes

$$\frac{\partial_\Omega\zeta_n}{\partial t}-\Omega\frac{\partial\zeta_n}{\partial\lambda}-\Omega\zeta_s=-\frac{\partial}{\partial z}(-\mathbf{v}_h\cdot\nabla_h v_s)-\frac{\partial}{\partial z}\left(-w\frac{\partial v_s}{\partial z}\right)+\frac{\partial}{\partial s}(-\mathbf{v}\cdot\nabla w)+f\frac{\partial(v_n-v_{gn})}{\partial z}+\hat{\mathbf{n}}\cdot\nabla p\times\nabla\alpha+\hat{\mathbf{n}}\cdot\nabla\times\mathbf{F}. \tag{B8}$$

Note that even though the second and third term of the left-hand side of Eq. (B8) can cause local changes of ζ_n, these terms, however, do not affect the volume-averaged tendency $\partial_\Omega\langle\zeta_n\rangle/\partial t$, because $\langle\partial\zeta_n/\partial\lambda\rangle=0$ and $\langle\zeta_s\rangle=0$. As a result, taking the volume average of Eq. (B8) yields

$$\frac{d\zeta_n}{dt}=-\left\langle\frac{\partial}{\partial z}(-\mathbf{v}_h\cdot\nabla_h v_s)\right\rangle-\left\langle\frac{\partial}{\partial z}\left(-w\frac{\partial v_s}{\partial z}\right)\right\rangle+\left\langle\frac{\partial}{\partial s}(-\mathbf{v}\cdot\nabla w)\right\rangle+f\left\langle\frac{\partial(v_n-v_{gn})}{\partial z}\right\rangle+\langle\hat{\mathbf{n}}\cdot\nabla p\times\nabla\alpha\rangle+\langle\hat{\mathbf{n}}\cdot\nabla\times\mathbf{F}\rangle. \tag{B9}$$

Similarly, if we take the dot product of Eq. (B6) with $\hat{\mathbf{s}}$,

$$\hat{\mathbf{s}}\cdot\frac{\partial}{\partial t}(\boldsymbol{\zeta}_a)=\frac{\partial_\Omega}{\partial t}(\zeta_s)-\Omega\frac{\partial\zeta_s}{\partial\lambda}+\Omega\zeta_n, \tag{B10}$$

we get

$$\frac{\partial_\Omega}{\partial t}(\zeta_s) - \Omega\frac{\partial\zeta_s}{\partial\lambda} + \Omega\zeta_n = \frac{\partial}{\partial z}(-\mathbf{v}_h\cdot\nabla_h v_n) + \frac{\partial}{\partial z}\left(-w\frac{\partial v_n}{\partial z}\right) - \frac{\partial}{\partial n}(-\mathbf{v}\cdot\nabla w) + f\frac{\partial(v_s - v_{gs})}{\partial z} + \hat{\mathbf{s}}\cdot\nabla p\times\nabla\alpha + \hat{\mathbf{s}}\cdot\nabla\times\mathbf{F}. \tag{B11}$$

Taking the volume integral, and noting that $(d\langle\zeta_s\rangle/dt) = 0$ and $\langle\partial\zeta_s/\partial\lambda\rangle = 0$,

$$\Omega\langle\zeta_n\rangle = \left\langle\frac{\partial}{\partial z}(-\mathbf{v}_h\cdot\nabla_h v_n)\right\rangle + \left\langle\frac{\partial}{\partial z}\left(-w\frac{\partial v_n}{\partial z}\right)\right\rangle - \left\langle\frac{\partial}{\partial n}(-\mathbf{v}\cdot\nabla w)\right\rangle + f\left\langle\frac{\partial(v_s - v_{gs})}{\partial z}\right\rangle + \langle\hat{\mathbf{s}}\cdot\nabla p\times\nabla\alpha\rangle + \langle\hat{\mathbf{s}}\cdot\nabla\times\mathbf{F}\rangle. \tag{B12}$$

Equations (B9) and (B12) are the component vorticity equations in this rotating coordinate that we use in this study to analyze changes in the magnitude and direction of the volume-averaged horizontal vorticity $\langle\boldsymbol{\zeta}_h\rangle$.

REFERENCES

Alland, J. J., B. H. Tang, K. L. Corbosiero, and G. H. Bryan, 2021a: Combined effects of midlevel dry air and vertical wind shear on tropical cyclone development. Part I: Downdraft ventilation. *J. Atmos. Sci.*, **78**, 763–782, https://doi.org/10.1175/JAS-D-20-0054.1.

——, ——, ——, and ——, 2021b: Combined effects of midlevel dry air and vertical wind shear on tropical cyclone development. Part II: Radial ventilation. *J. Atmos. Sci.*, **78**, 783–796, https://doi.org/10.1175/JAS-D-20-0055.1.

Alvey, G. R., E. Zipser, and J. Zawislak, 2020: How does Hurricane Edouard (2014) evolve toward symmetry before rapid intensification? A high-resolution ensemble study. *J. Atmos. Sci.*, **77**, 1329–1351, https://doi.org/10.1175/JAS-D-18-0355.1.

Bhatia, K. T., and D. S. Nolan, 2013: Relating the skill of tropical cyclone intensity forecasts to the synoptic environment. *Wea. Forecasting*, **28**, 961–980, https://doi.org/10.1175/WAF-D-12-00110.1.

Black, P. G., and R. A. Anthes, 1971: On the asymmetric structure of the tropical cyclone outflow layer. *J. Atmos. Sci.*, **28**, 1348–1366, https://doi.org/10.1175/1520-0469(1971)028<1348:OTASOT>2.0.CO;2.

Boehm, A. M., and M. M. Bell, 2021: Retrieved thermodynamic structure of Hurricane Rita (2005) from airborne multi–Doppler radar data. *J. Atmos. Sci.*, **78**, 1583–1605, https://doi.org/10.1175/JAS-D-20-0195.1.

Braun, S. A., M. T. Montgomery, K. J. Mallen, and P. D. Reasor, 2010: Simulation and interpretation of the genesis of Tropical Storm Gert (2005) as part of the NASA Tropical Cloud Systems and Processes Experiment. *J. Atmos. Sci.*, **67**, 999–1025, https://doi.org/10.1175/2009JAS3140.1.

Bryan, G. H., 2012: Effects of surface exchange coefficients and turbulence length scales on the intensity and structure of numerically simulated hurricanes. *Mon. Wea. Rev.*, **140**, 1125–1143, https://doi.org/10.1175/MWR-D-11-00231.1.

——, and J. M. Fritsch, 2002: A benchmark simulation for moist nonhydrostatic numerical models. *Mon. Wea. Rev.*, **130**, 2917–2928, https://doi.org/10.1175/1520-0493(2002)130<2917:ABSFMN>2.0.CO;2.

——, and R. Rotunno, 2009: The maximum intensity of tropical cyclones in axisymmetric numerical model simulations. *Mon. Wea. Rev.*, **137**, 1770–1789, https://doi.org/10.1175/2008MWR2709.1.

——, and H. Morrison, 2012: Sensitivity of a simulated squall line to horizontal resolution and parameterization of microphysics. *Mon. Wea. Rev.*, **140**, 202–225, https://doi.org/10.1175/MWR-D-11-00046.1.

Charney, J. G., 1955: The use of primitive equations of motion in numerical prediction. *Tellus*, **7**, 22–26, https://doi.org/10.3402/tellusa.v7i1.8772.

Chen, H., and S. G. Gopalakrishnan, 2015: A study on the asymmetric rapid intensification of Hurricane Earl (2010) using the HWRF system. *J. Atmos. Sci.*, **72**, 531–550, https://doi.org/10.1175/JAS-D-14-0097.1.

Chen, S. S., J. A. Knaff, and F. D. Marks, 2006: Effects of vertical wind shear and storm motion on tropical cyclone rainfall asymmetries deduced from TRMM. *Mon. Wea. Rev.*, **134**, 3190–3208, https://doi.org/10.1175/MWR3245.1.

Chen, X., Y. Wang, J. Fang, and M. Xue, 2018: A numerical study on rapid intensification of Typhoon Vicente (2012) in the South China Sea. Part II: Roles of inner-core processes. *J. Atmos. Sci.*, **75**, 235–255, https://doi.org/10.1175/JAS-D-17-0129.1.

Corbosiero, K. L., and J. Molinari, 2002: The effects of vertical wind shear on the distribution of convection in tropical cyclones. *Mon. Wea. Rev.*, **130**, 2110–2123, https://doi.org/10.1175/1520-0493(2002)130<2110:TEOVWS>2.0.CO;2.

Dai, Y., J. Majumdar, and D. S. Nolan, 2019: The outflow–rainband relationship induced by environmental flow around tropical cyclones. *J. Atmos. Sci.*, **76**, 1845–1863, https://doi.org/10.1175/JAS-D-18-0208.1.

——, ——, and ——, 2021: Tropical cyclone resistance to strong environmental shear. *J. Atmos. Sci.*, **78**, 1275–1293, https://doi.org/10.1175/JAS-D-20-0231.1.

Davis, C. A., and K. A. Emanuel, 1991: Potential vorticity diagnosis of cyclogenesis. *Mon. Wea. Rev.*, **119**, 1929–1953, https://doi.org/10.1175/1520-0493(1991)119<1929:PVDOC>2.0.CO;2.

——, S. C. Jones, and M. Riemer, 2008: Hurricane vortex dynamics during Atlantic extratropical transition. *J. Atmos. Sci.*, **65**, 714–736, https://doi.org/10.1175/2007JAS2488.1.

DeHart, J. C., R. A. Houze Jr., and R. F. Rogers, 2014: Quadrant distribution of tropical cyclone inner-core kinematics in relation to environmental shear. *J. Atmos. Sci.*, **71**, 2713–2732, https://doi.org/10.1175/JAS-D-13-0298.1.

DeMaria, M., 1996: The effect of vertical shear on tropical cyclone intensity change. *J. Atmos. Sci.*, **53**, 2076–2088, https://doi.org/10.1175/1520-0469(1996)053<2076:TEOVSO>2.0.CO;2.

——, and J. Kaplan, 1994: A Statistical Hurricane Intensity Prediction Scheme (SHIPS) for the Atlantic basin. *Wea. Forecasting*, **9**, 209–220, https://doi.org/10.1175/1520-0434(1994)009<0209:ASHIPS>2.0.CO;2.

——, M. Mainelli, L. K. Shay, J. A. Knaff, and J. Kaplan, 2005: Further improvements to the Statistical Hurricane Intensity Prediction Scheme (SHIPS). *Wea. Forecasting*, **20**, 531–543, https://doi.org/10.1175/WAF862.1.

Didlake, A. C., Jr., and R. A. Houze Jr., 2013: Dynamics of the stratiform sector of a tropical cyclone rainband. *J. Atmos. Sci.*, **70**, 1891–1911, https://doi.org/10.1175/JAS-D-12-0245.1.

Donelan, M. A., B. K. Haus, N. Reul, W. J. Plant, M. Stiassnie, H. C. Graber, O. B. Brown, and E. S. Saltzman, 2004: On the limiting aerodynamic roughness of the ocean in very strong winds. *Geophys. Res. Lett.*, **31**, L18306, https://doi.org/10.1029/2004GL019460.

Drennan, W. M., J. A. Zhang, J. R. French, C. McCormick, and P. G. Black, 2007: Turbulent fluxes in the hurricane boundary layer. Part II: Latent heat flux. *J. Atmos. Sci.*, **64**, 1103–1115, https://doi.org/10.1175/JAS3889.1.

Dunion, J. P., 2011: Rewriting the climatology of the tropical North Atlantic and Caribbean Sea atmosphere. *J. Climate*, **24**, 893–908, https://doi.org/10.1175/2010JCLI3496.1.

Elsberry, R. L., and R. A. Jeffries, 1996: Vertical wind shear influences on tropical cyclone formation and intensification during TCM-92 and TCM-93. Mon. Wea. Rev., **124**, 1374–1387, https://doi.org/10.1175/1520-0493(1996)124<1374:VWSIOT>2.0.CO;2.

Fairall, C. W., E. F. Bradley, J. E. Hare, A. A. Grachev, and J. B. Edson, 2003: Bulk parameterization of air–sea fluxes: Updates and verification for the COARE algorithm. *J. Climate*, **16**, 571–591, https://doi.org/10.1175/1520-0442(2003)016<0571:BPOASF>2.0.CO;2.

Finocchio, P. M., and S. J. Majumdar, 2017: The predictability of idealized tropical cyclones in environments with time-varying vertical wind shear. *J. Adv. Model. Earth Syst.*, **9**, 2836–2862, https://doi.org/10.1002/2017MS001168.

—— and R. Rios-Berrios, 2021: The intensity- and size-dependent response of tropical cyclones to increasing vertical wind shear. *J. Atmos. Sci.*, **78**, 3673–3690, https://doi.org/10.1175/JAS-D-21-0126.1.

——, S. J. Majumdar, D. S. Nolan, and M. Iskandarani, 2016: Idealized tropical cyclone responses to the height and depth of environmental vertical wind shear. *Mon. Wea. Rev.*, **144**, 2155–2175, https://doi.org/10.1175/MWR-D-15-0320.1.

Fischer, M. S., R. F. Rogers, and P. D. Reasor, 2021: Relationships between vortex tilt, convective structure, and intensity change in early-stage tropical cyclones. *34th Conf. on Hurricanes and Tropical Meteorology*, Online, Amer. Meteor. Soc., 5B.6, https://ams.confex.com/ams/34HURR/meetingapp.cgi/Paper/373691.

Frank, W. M., and E. A. Ritchie, 1999: Effects of environmental flow upon tropical cyclone structure. *Mon. Wea. Rev.*, **127**, 2044–2061, https://doi.org/10.1175/1520-0493(1999)127<2044:EOEFUT>2.0.CO;2.

——, and ——, 2001: Effects of vertical wind shear on the intensity and structure of numerically simulated hurricanes. *Mon. Wea. Rev.*, **129**, 2249–2269, https://doi.org/10.1175/1520-0493(2001)129<2249:EOVWSO>2.0.CO;2.

Gjorgjievska, S., and D. J. Raymond, 2014: Interaction between dynamics and thermodynamics during tropical cyclogenesis. *Atmos. Chem. Phys.*, **14**, 3065–3082, https://doi.org/10.5194/acp-14-3065-2014.

Haltiner, G. J., and R. T. Williams, 1980: *Numerical Prediction and Dynamic Meteorology*. 2nd ed. Wiley and Sons, 477 pp.

Hazelton, A. T., X. Zhang, S. Gopalakrishnan, W. Ramstrom, F. Marks, and J. A. Zhang, 2020: High-resolution ensemble HFV3 forecasts of Hurricane Michael (2018): Rapid intensification in shear. *Mon. Wea. Rev.*, **148**, 2009–2032, https://doi.org/10.1175/MWR-D-19-0275.1.

Hendricks, E. A., S. P. Melinda, B. Fu, and T. Li, 2010: Quantifying environmental control on tropical cyclone intensity change. *Mon. Wea. Rev.*, **138**, 3243–3271, https://doi.org/10.1175/2010MWR3185.1.

Holton, J. R., 1992: *An Introduction to Dynamic Meteorology*. 3rd ed. Academic Press, 511 pp.

Hong, S.-Y., Y. Noh, and J. Dudhia, 2006: A new vertical diffusion package with an explicit treatment of entrainment processes. *Mon. Wea. Rev.*, **134**, 2318–2341, https://doi.org/10.1175/MWR3199.1.

Iacono, M. J., J. S. Delamere, E. J. Mlawer, M. W. Shephard, S. A. Clough, and W. D. Collins, 2008: Radiative forcing by long-lived greenhouse gases: Calculations with the AER radiative transfer models. *J. Geophys. Res.*, **113**, D13103, https://doi.org/10.1029/2008JD009944.

Jones, S. C., 1995: The evolution of vortices in vertical shear. I: Initially barotropic vortices. *Quart. J. Roy. Meteor.*, **121**, 821–851, https://doi.org/10.1002/qj.49712152406.

——, 2000: The evolution of vortices in vertical shear. II: Large-scale asymmetries. *Quart. J. Roy. Meteor. Soc.*, **126**, 3137–3159, https://doi.org/10.1002/qj.49712657008.

Kaplan, J., and M. DeMaria, 2003: Large-scale characteristics of rapidly intensifying tropical cyclones in the North Atlantic basin. *Wea. Forecasting*, **18**, 1093–1108, https://doi.org/10.1175/1520-0434(2003)018<1093:LCORIT>2.0.CO;2.

Krishnamurti, T. N., 1968: A diagnostic balance model for studies of weather systems of low and high latitudes, Rossby number less than 1. *Mon. Wea. Rev.*, **96**, 197–207, https://doi.org/10.1175/1520-0493(1968)096<0197:ADBMFS>2.0.CO;2.

Miyamoto, Y., and D. S. Nolan, 2018: Structural changes preceding rapid intensification in tropical cyclones as shown in a large ensemble of idealized simulations. *J. Atmos. Sci.*, **75**, 555–569, https://doi.org/10.1175/JAS-D-17-0177.1.

Molinari, J., D. Vollaro, and K. L. Corbosiero, 2004: Tropical cyclone formation in a sheared environment: A case study. *J. Atmos. Sci.*, **61**, 2493–2509, https://doi.org/10.1175/JAS3291.1.

Nguyen, L. T., and J. Molinari, 2015: Simulation of the downshear reformation of a tropical cyclone. *J. Atmos. Sci.*, **72**, 4529–4551, https://doi.org/10.1175/JAS-D-15-0036.1.

——, ——, and D. Thomas, 2014: Evaluation of tropical cyclone center identification methods in numerical models. *Mon. Wea. Rev.*, **142**, 4326–4339, https://doi.org/10.1175/MWR-D-14-00044.1.

Onderlinde, M. J., and D. S. Nolan, 2017: The tropical cyclone response to changing wind shear using the method of time-varying point-downscaling. *J. Adv. Model. Earth Syst.*, **9**, 908–931, https://doi.org/10.1002/2016MS000796.

Paterson, L. A., B. N. Hanstrum, N. E. Davidson, and H. C. Weber, 2005: Influence of environmental vertical wind shear on the intensity of hurricane-strength tropical cyclones in the Australian region. *Mon. Wea. Rev.*, **133**, 3644–3660, https://doi.org/10.1175/MWR3041.1.

Polvani, L. M., 1991: Two-layer geostrophic vortex dynamics. Part 2. Alignment and two-layer V-states. *J. Fluid Mech.*, **225**, 241–270, https://doi.org/10.1017/S0022112091002045.

Raymond, D. J., 1992: Nonlinear balance and potential-vorticity thinking at large Rossby number. *Quart. J. Roy. Meteor. Soc.*, **118**, 987–1015, https://doi.org/10.1002/qj.49711850708.

——, S. Gjorgjievska, S. Sessions, and Ž. Fuchs, 2014: Tropical cyclogenesis and mid-level vorticity. *Aust. Meteor. Oceanogr.*, **64**, 11–25, https://doi.org/10.22499/2.6401.003.

Reasor, P. D., and M. T. Montgomery, 2001: Three-dimensional alignment and corotation of weak, TC-like vortices via linear vortex Rossby waves. *J. Atmos. Sci.*, **58**, 2306–2330, https://doi.org/10.1175/1520-0469(2001)058<2306:TDAACO>2.0.CO;2.

——, and M. D. Eastin, 2012: Rapidly intensifying Hurricane Guillermo (1997). Part II: Resilience in shear. *Mon. Wea. Rev.*, **140**, 425–444, https://doi.org/10.1175/MWR-D-11-00080.1.

——, and M. T. Montgomery, 2015: Evaluation of a heuristic model for tropical cyclone resilience. *J. Atmos. Sci.*, **72**, 1765–1782, https://doi.org/10.1175/JAS-D-14-0318.1.

——, ——, F. D. Marks, and J. F. Gamache, 2000: Low-wavenumber structure and evolution of the hurricane inner core observed by airborne dual-Doppler radar. *Mon. Wea. Rev.*, **128**, 1653–1680, https://doi.org/10.1175/1520-0493(2000)128<1653:LWSAEO>2.0.CO;2.

——, ——, and L. D. Grasso, 2004: A new look at the problem of tropical cyclones in vertical shear flow: Vortex resiliency. *J. Atmos. Sci.*, **61**, 3–22, https://doi.org/10.1175/1520-0469(2004)061<0003:ANLATP>2.0.CO;2.

——, R. Rogers, and S. Lorsolo, 2013: Environmental flow impacts on tropical cyclone structure diagnosed from airborne Doppler radar composites. *Mon. Wea. Rev.*, **141**, 2949–2969, https://doi.org/10.1175/MWR-D-12-00334.1.

Riemer, M., and M. T. Montgomery, 2011: Simple kinematic models for the environmental interaction of tropical cyclones in vertical wind shear. *Atmos. Chem. Phys.*, **11**, 9395–9414, https://doi.org/10.5194/acp-11-9395-2011.

——, and M. E. Nicholls, 2010: A new paradigm for intensity modification of tropical cyclones: Thermodynamic impact of vertical wind shear on the inflow layer. *Atmos. Chem. Phys.*, **10**, 3163–3188, https://doi.org/10.5194/acp-10-3163-2010.

——, M. T. Montgomery, and M. E. Nicholls, 2013: Further examination of the thermodynamic modification of the inflow layer of tropical cyclones by vertical wind shear. *Atmos. Chem. Phys.*, **13**, 327–346, https://doi.org/10.5194/acp-13-327-2013.

Rios-Berrios, R., 2020: Impacts of radiation and cold pools on the intensity and vortex tilt of weak tropical cyclones interacting with vertical wind shear. *J. Atmos. Sci.*, **77**, 669–689, https://doi.org/10.1175/JAS-D-19-0159.1.

——, and R. D. Torn, 2017: Climatological analysis of tropical cyclone intensity changes under moderate vertical wind shear. *Mon. Wea. Rev.*, **145**, 1717–1738, https://doi.org/10.1175/MWR-D-16-0350.1.

——, ——, and C. A. Davis, 2016a: An ensemble approach to investigate tropical cyclone intensification in sheared environments. Part I: Katia (2011). *J. Atmos. Sci.*, **73**, 71–93, https://doi.org/10.1175/JAS-D-15-0052.1.

——, ——, and ——, 2016b: An ensemble approach to investigate tropical cyclone intensification in sheared environments. Part II: Ophelia (2011). *J. Atmos. Sci.*, **73**, 1555–1575, https://doi.org/10.1175/JAS-D-15-0245.1.

——, C. A. Davis, and R. D. Torn, 2018: A hypothesis for the intensification of tropical cyclones under moderate vertical wind shear. *J. Atmos. Sci.*, **75**, 4149–4173, https://doi.org/10.1175/JAS-D-18-0070.1.

Rogers, R. F., J. A. Zhang, J. Zawislak, H. Jiang, G. R. Alvey III, E. J. Zipser, and S. N. Stevenson, 2016: Observations of the structure and evolution of Hurricane Edouard (2014) during intensity change. Part II: Kinematic structure and the distribution of deep convection. *Mon. Wea. Rev.*, **144**, 3355–3376, https://doi.org/10.1175/MWR-D-16-0017.1.

Rotunno, R., and K. A. Emanuel, 1987: An air–sea interaction theory for tropical cyclones. Part II: Evolutionary study using a nonhydrostatic axisymmetric numerical model. *J. Atmos. Sci.*, **44**, 542–561, https://doi.org/10.1175/1520-0469(1987)044<0542:AAITFT>2.0.CO;2.

Ryglicki, D. R., and R. E. Hart, 2015: An investigation of center finding techniques for tropical cyclones in mesoscale models. *J. Appl. Meteor. Climatol.*, **54**, 825–846, https://doi.org/10.1175/JAMC-D-14-0106.1.

——, J. H. Cossuth, D. Hodyss, and J. D. Doyle, 2018a: The unexpected rapid intensification of tropical cyclones in moderate vertical wind shear. Part I: Overview and observations. *Mon. Wea. Rev.*, **146**, 3773–3800, https://doi.org/10.1175/MWR-D-18-0020.1.

——, J. D. Doyle, Y. Jin, D. Hodyss, and J. H. Cossuth, 2018b: The unexpected rapid intensification of tropical cyclones in moderate vertical wind shear. Part II: Vortex tilt. *Mon. Wea. Rev.*, **146**, 3801–3825, https://doi.org/10.1175/MWR-D-18-0021.1.

——, ——, D. Hodyss, J. H. Cossuth, Y. Jin, K. C. Viner, and J. M. Schmidt, 2019: The unexpected rapid intensification of tropical cyclones in moderate vertical wind shear. Part III: Outflow–environment interaction. *Mon. Wea. Rev.*, **147**, 2919–2940, https://doi.org/10.1175/MWR-D-18-0370.1.

Schecter, D. A., 2015: Response of a simulated hurricane to misalignment forcing compared to the predictions of a simple theory. *J. Atmos. Sci.*, **72**, 1235–1260, https://doi.org/10.1175/JAS-D-14-0149.1.

——, 2020: Distinct intensification pathways for a shallow-water vortex subjected to asymmetric "diabatic" forcing. *Dyn. Atmos. Oceans*, **91**, 101156, https://doi.org/10.1016/j.dynatmoce.2020.101156.

——, 2022: Intensification of tilted tropical cyclones over relatively cool and warm oceans in idealized numerical simulations. *J. Atmos. Sci.*, **79**, 485–512, https://doi.org/10.1175/JAS-D-21-0051.1.

——, and K. Menelaou, 2020: Development of a misaligned tropical cyclone. *J. Atmos. Sci.*, **77**, 79–111, https://doi.org/10.1175/JAS-D-19-0074.1.

——, M. T. Montgomery, and P. D. Reasor, 2002: A theory for the vertical alignment of a quasigeostrophic vortex. *J. Atmos. Sci.*, **59**, 150–168, https://doi.org/10.1175/1520-0469(2002)059<0150:ATFTVA>2.0.CO;2.

Sprenger, M., and H. Wernli, 2015: The LAGRANTO Lagrangian analysis tool—Version 2.0. *Geosci. Model Dev.*, **8**, 2569–2586, https://doi.org/10.5194/gmd-8-2569-2015.

Stevenson, S. N., K. L. Corbosiero, and J. Molinari, 2014: The convective evolution and rapid intensification of Hurricane Earl (2010). *Mon. Wea. Rev.*, **142**, 4364–4380, https://doi.org/10.1175/MWR-D-14-00078.1.

Tang, B., and K. Emanuel, 2010: Midlevel ventilation's constraint on tropical cyclone intensity. *J. Atmos. Sci.*, **67**, 1817–1830, https://doi.org/10.1175/2010JAS3318.1.

——, and ——, 2012a: Sensitivity of tropical cyclone intensity to ventilation in an axisymmetric model. *J. Atmos. Sci.*, **69**, 2394–2413, https://doi.org/10.1175/JAS-D-11-0232.1.

——, and ——, 2012b: A ventilation index for tropical cyclones. *Bull. Amer. Meteor. Soc.*, **93**, 1901–1912, https://doi.org/10.1175/BAMS-D-11-00165.1.

Tao, D., and F. Zhang, 2014: Effect of environmental shear, sea-surface temperature, and ambient moisture on the formation and predictability of tropical cyclones: An ensemble-mean perspective. *J. Adv. Model. Earth Syst.*, **6**, 384–404, https://doi.org/10.1002/2014MS000314.

——, and ——, 2015: Effects of vertical wind shear on the predictability of tropical cyclones: Practical versus intrinsic limit.

J. Adv. Model. Earth Syst., **7**, 1534–1553, https://doi.org/10.1002/2015MS000474.

Vico, F., L. Greengard, and M. Ferrando, 2016: Fast convolution with free-space Green's functions. *J. Comput. Phys.*, **323**, 191–203, https://doi.org/10.1016/j.jcp.2016.07.028.

Wadler, J. B., R. F. Rogers, and P. D. Reasor, 2018: The relationship between spatial variations in the structure of convective bursts and tropical cyclone intensification as determined by airborne Doppler radar. *Mon. Wea. Rev.*, **146**, 761–780, https://doi.org/10.1175/MWR-D-17-0213.1.

Wang, Y., and G. J. Holland, 1996: Tropical cyclone motion and evolution in vertical shear. *J. Atmos. Sci.*, **53**, 3313–3332, https://doi.org/10.1175/1520-0469(1996)053<3313:TCMAEI>2.0.CO;2.

Wernli, B. H., and H. C. Davies, 1997: A Lagrangian-based analysis of extratropical cyclones. I: The method and some applications. *Quart. J. Roy. Meteor. Soc.*, **123**, 467–489, https://doi.org/10.1002/qj.49712353811.

Zhang, F., and D. Tao, 2013: Effects of vertical wind shear on the predictability of tropical cyclones. *J. Atmos. Sci.*, **70**, 975–983, https://doi.org/10.1175/JAS-D-12-0133.1.